Chemical control over hemi-indigo photoswitches

Duindam, N.

CHAPTER 2

Monodirectional Photocycle Drives Proton Translocation

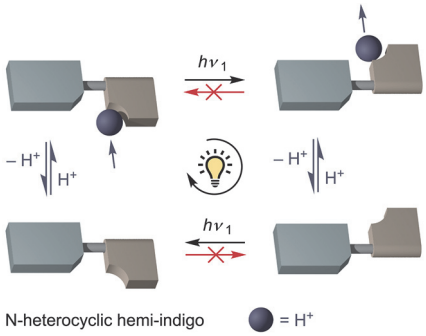

Photoisomerization of retinal is pivotal to ion translocation across the bacterial membrane and has served as inspiration for the development of artificial molecular switches and machines. Light-driven synthetic systems in which a macrocyclic component transits along a nonsymmetric axle in a specific direction have been reported, however, unidirectional and repetitive translocation of protons has not been achieved. Herein, we describe unique protonation-controlled isomerization behavior for hemi-indigo dyes bearing N-heterocycles, featuring intramolecular hydrogen bonds. Light-induced isomerization from the *Z*-to-*E* isomer is unlocked when protonated, while reverse *E*-to-*Z* photoisomerization occurs in the neutral state. As a consequence, associated protons are displaced in a preferred direction with respect to the photoswitchable scaffold. These results will prove critical in developing artificial systems in which concentration gradients can be effectively generated using (solar) light energy.

The work that is described in this chapter has been published:

N. Duindam, M. van Dongen, M. A. Siegler, S. J. Wezenberg, *J. Am. Chem. Soc.* **2023**, *145*, 21020-21026

2.1 Introduction

In bacteriorhodopsin, photochemical all-*trans* to 13-*cis* double-bond isomerization of retinal's protonated Schiff base is at the basis of a proton translocation event.[1-3] Release of protons to the extracellular medium and reprotonation from the cytoplasm create a concentration gradient, which serves as an energy reservoir to produce ATP. Artificial systems that – to some extent – imitate such function[4-6] may provide a new perspective on solar energy conversion and storage. Hence, synthetic tools to drive substrate translocation are highly sought after, for example, within the field of molecular machines.[7-11] Indeed, pseudorotaxane structures in which a macrocyclic ring moves repeatedly along a nonsymmetric axle in a specific direction have been reported.[12-18] Further, controlled displacement of a proton by photoswitchable systems has been shown.[19] However, repetitive unidirectional translocation of protons has not been achieved to date, while it would be of particular interest for developing artificial light-driven molecular pumps.[17-18]

Taking inspiration from retinal isomerization, one could think of transporting protons by association with a small-molecule photoswitch. However, once under continuous irradiation a photostationary state (PSS) has been established, the rates at which the photoaddressable isomers interconvert into each other are equal. Although forwards and backwards excited state isomerization paths are different,[20,21] an associated proton will then be taken in both switching directions, undoing repetitive displacement. We envisioned that if protonation can activate one of the photoswitching directions and suppress the other, repetitive unidirectional translocation becomes viable. In other words, the proton would carry the information that dictates in which direction photoisomerization occurs and hence, the system operates according to an information ratchet mechanism.[9,22] As a consequence, machine-like pumping behavior would emerge from a simple molecular photoswitch by harnessing the continuous interconversion between isomers under non-stop irradiation with one and the same wavelength (or a broad spectrum) of light.

We considered hemi-indigo to be suitable for the design of a proton information ratchet for several reasons. While it recently regained attention for its use as molecular photoswitch,[23] its pyridyl derivative was found to not undergo *Z*-to-*E* photoisomerization.[24,25] Conversely, *E*-to-*Z* photoisomerization of some structurally related indole-containing hemi-thioindigo derivatives was found to be suppressed, which was explained by the formation of a strong intramolecular hydrogen bond.[26,27] It has further been shown that incorporation of a pyrrolic ring can energetically favor the otherwise metastable *E*-isomer of hemi-(thio)indigos owing to this intramolecular hydrogen bond formation.[24-28] Based on these findings, we hypothesized that protonation of N-heterocyclic hemi-indigos could enable

photoisomerization of the *Z*-isomer due to disruption of the intramolecular hydrogen bond. On the other hand, in the protonated state, an intramolecular hydrogen bond would be formed in the *E* isomer, which could potentially suppress the photochemical isomerization. In addition, we envisioned that this intramolecular hydrogen bond formation and disruption by (de)protonation could be used to induce reversible thermally activated double bond isomerization, which so far has only been achieved in hydrazones[29,30] and indigo-derived imines.[31]

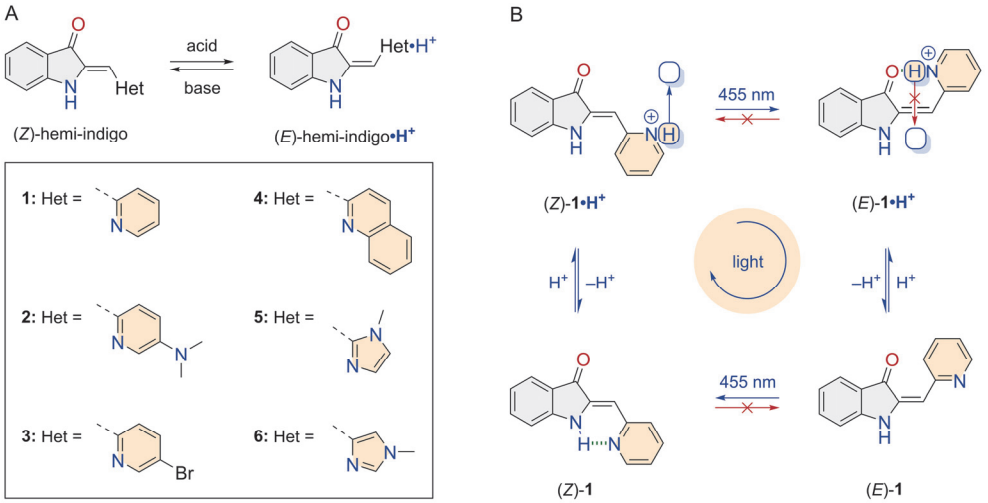

Scheme 1. (A) Acid/base-controlled thermally activated double bond isomerization in hemi-indigos **1**-**6** and (B) sequence-specific monocyclic interconversion under light irradiation in the presence of acid shown for pyridyl-derivative **1**. The species are interconverted in the order: (*Z*)-**1**→(*Z*)-**1**·H$^+$→(*E*)-**1**·H$^+$→(*E*)-**1**→(*Z*)-**1**. As the forward isomerization takes place in the protonated state and the backwards isomerization occurs after deprotonation, protons are displaced effectively (from bottom to top with respect to hemi-indigo as indicated by the blue arrow) under continuous 455 nm irradiation.

Herein, it is demonstrated for six different N-heterocyclic hemi-indigos (Scheme 1A) that the forward *Z*-to-*E* photoisomerization takes place only when protonated, while the reverse *E*-to-*Z* photoisomerization occurs in the neutral state. One-way and virtually quantitative conversion is therefore attained in single and opposite directions for the neutral and protonated species. Since in the presence of acid, the neutral and protonated species are in equilibrium, they are interchanged photochemically in a specific order under irradiation with one and the same wavelength of light as is illustrated in Scheme 1B. We came to the realization that associated protons are thereby displaced in one direction with respect to the photoswitchable hemi-indigo scaffold. In addition, under conditions different than those in the irradiation experiments, quantitative and reversible conversion from the *Z*-to-*E* isomer

and *vice versa* is induced by acid and base, respectively, and these hemi-indigos thus constitute a new class of pH-responsive switches.

2.2 Energy Minimization by DFT

To gain insight into the stabilizing effect of intramolecular hydrogen bonding in the ground state, the geometries of possible isomers of hemi-indigo pyridyl derivative **1** were minimized by density functional theory (DFT, B3LYP/6-311++G(d,p) level of theory and an IEF-PCM $CHCl_3$ solvent model, Scheme E1). For the *E*- and the *Z*-isomers, in both their neutral and protonated states, two possible rotational isomers were considered. The energetically most favored conformations are depicted in Figure 1 alongside the relative energies. As anticipated, in (*Z*)-**1** a hydrogen bond is formed between the pyridyl nitrogen and the N–H atom of the 3-oxindole fragment [N(H)···N distance = 2.81 Å], which is not possible in (*E*)-**1**. Conversely, in the protonated state of the former isomer, the pyridinium nitrogen is rotated away from the N-H hydrogen bond donor and not involved in hydrogen bonding. Now instead, a stabilizing hydrogen bond can be formed in the *E*-isomer, i.e. between the pyridinium proton and the carbonyl oxygen atom [N(H)···O distance = 2.64 Å]. Owing mainly to this intramolecular hydrogen bond formation, there is a substantial thermodynamic preference for the *Z*- over the *E*-isomer in the neutral state (ΔG = 32.9 kJ mol^{-1}), whereas in the protonated state the *E*-isomer is considerably lower in energy (ΔG = –30.5 kJ mol^{-1}).

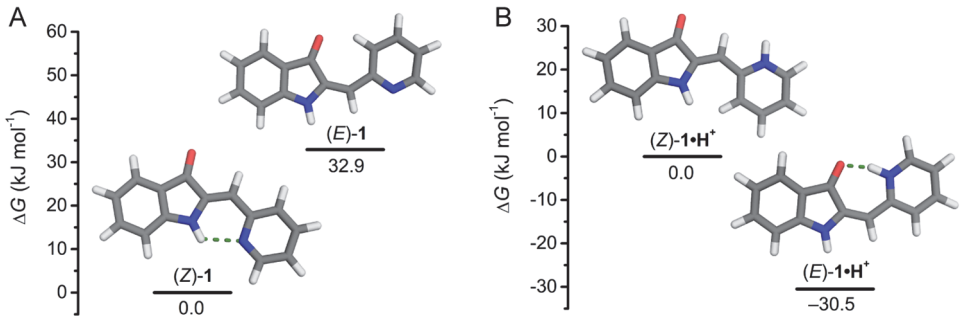

Figure 1. DFT-minimized geometries and plots of the relative Gibbs free energies; Color codes: hydrogen bond = green; O = red; N = blue.

2.3 Synthesis and Crystallographic Analysis

We then synthesized hemi-indigo **1** as well as derivatives **2**-**6**, which contain different N-heterocycles, through a condensation reaction of commercially available indoxyl acetate with the respective aldehydes (Scheme 2).[23,32] The imidazole rings in compounds **5** and **6** were methylated to avoid tautomerization. The desired products were obtained in good yields (65–82%) as the thermodynamically most stable *Z*-isomers (*Z*/*E* ratio >99%). The ^{1}H NMR spectra recorded in $CDCl_3$ revealed downfield-shifted NH-signals for all compounds (δ = 10.47–9.14 ppm) with respect to parent hemi-indigo containing a phenyl instead of the N-heterocyclic ring (**7**, δ = 6.82 ppm), which indicates involvement of the NH proton in hydrogen bonding with the nearest nitrogen atom of the N-heterocycles.

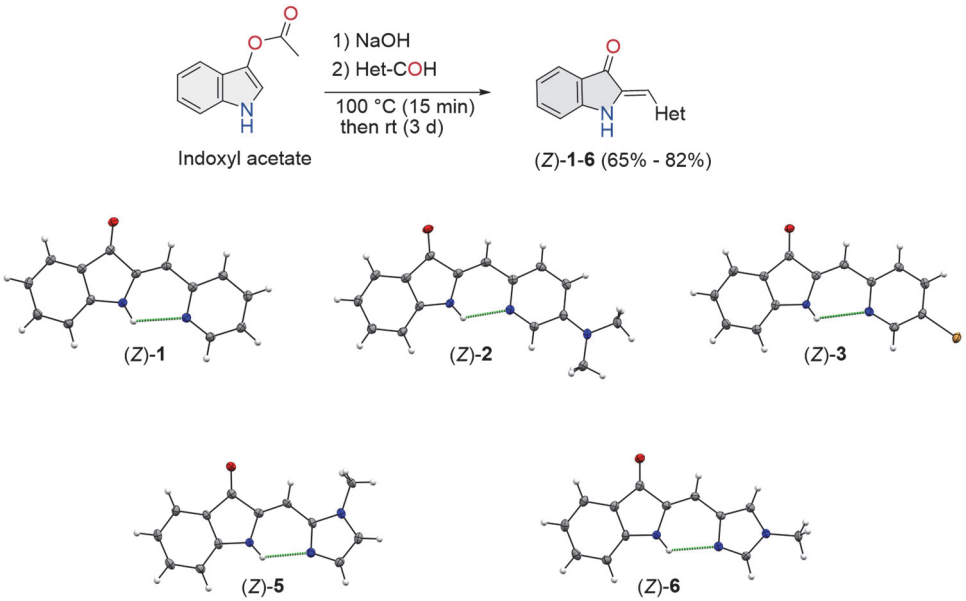

Scheme 2. Synthetic step towards hemi-indigos **1**-**6** and below the displacement ellipsoid plots (50% probability level, 110(2) K) of the products for which crystal structures were obtained.

All products, except quinolyl derivative **4**, were additionally characterized by single-crystal X-ray crystallography (Scheme 2). The solid-state structures are (as expected) of the energetically most stable *Z*-isomers. The structural similarity between these *Z*-isomers is high, i.e., the torsional angles between 3-oxindole and N-heterocycle moieties are all below 3° and the N(H)···N bond distances are found between 2.72–2.86 Å, which is within hydrogen bond range (Table E1). The presence of a stabilizing intramolecular hydrogen bond is thus supported in all cases. Important to note is that for (*Z*)-**1** this hydrogen bond distance (2.82 Å) is similar to the one in the DFT calculated structure (2.81 Å).

2.4 Acid-Induced Thermal Isomerization

Initially, it was studied if thermal isomerization to the *E*-isomer could occur upon protonation using ^{1}H NMR and UV-Vis spectroscopy. Incremental addition of trifluoroacetic acid (TFA, from 0-4 equiv.) to (*Z*)-**1** in $CDCl_3$ resulted in clear downfield shifting of all pyridyl ^{1}H NMR signals (H_j, H_i, H_h and H_g), indicative of protonation (Figure 2A). Concomitantly, the olefinic proton signal (H_f) shifted upfield, whereas for the aromatic 3-oxindole protons (H_{a-d}) only minor chemical shift changes were observed and the signal belonging to the NH-proton (H_e) shifted and broadened. At first, saturation seemed to be reached at around 4 equivalents, but when adding more TFA (from 4–40 equiv., Figure 2B) some of the chemical shift changes reversed, most notably for the pyridyl *ortho*-proton (H_g) and the olefinic proton (H_f), pointing at a secondary process. We hypothesized that it could be related to the solvation of an initially formed pyridinium-trifluoroacetate ion pair.[33] Indeed, when a ^{1}H NMR titration experiment was carried out with pyridine instead of (*Z*)-**1**, a similar trend was observed. We therefore presume that the extent of ion-pairing between (*Z*)-**1**·$\mathbf{H}^+$ and the trifluoroacetate counteranion is reduced when more TFA is present, accounting for the reverse in chemical shift changes beyond the addition of 4 equiv. in the titration.

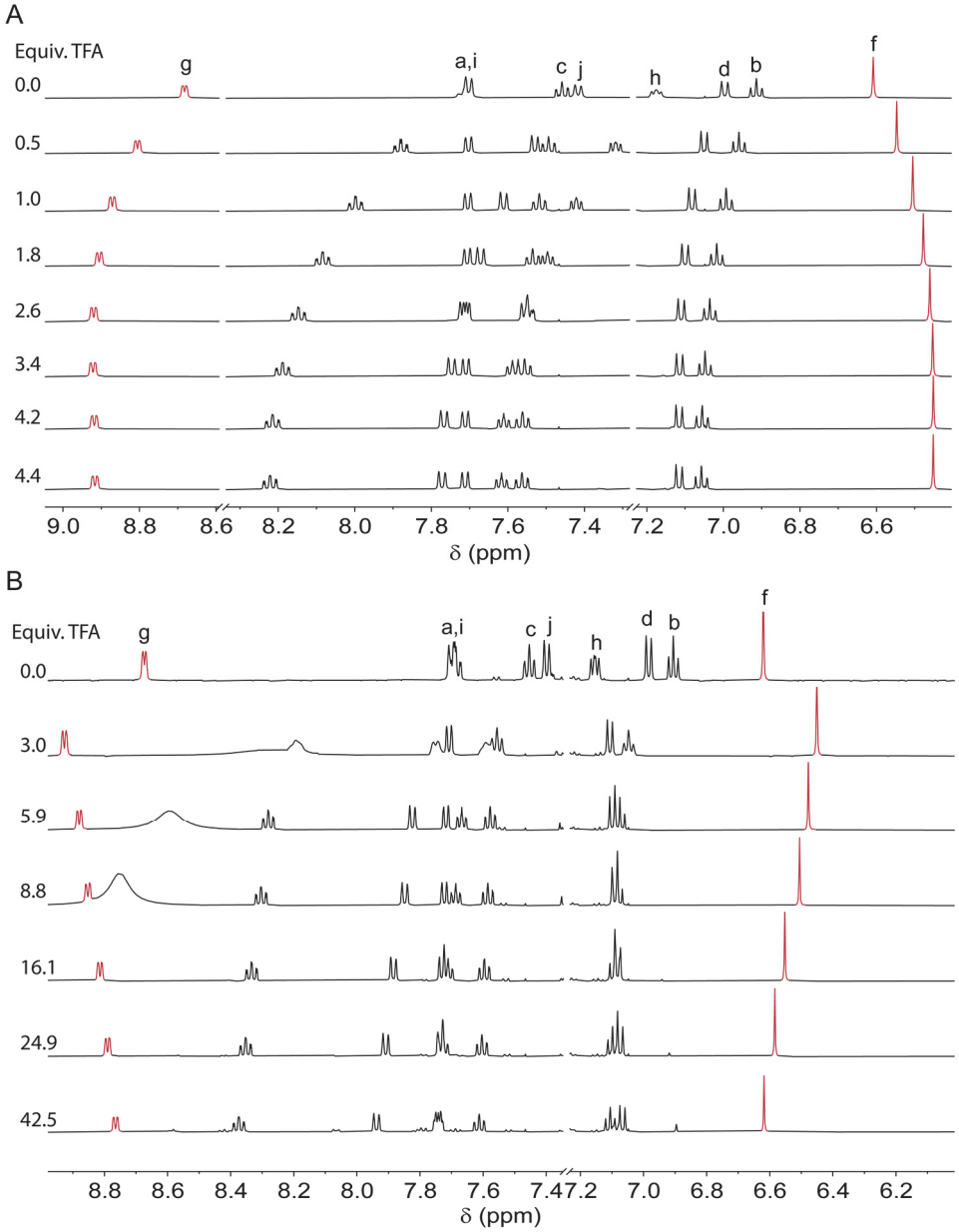

Figure 2. Spectral changes in selected regions in the ^{1}H NMR spectrum (500 MHz) upon gradual addition of (A) TFA (0-4 equiv., 0.18 M in $CDCl_3$) to (*Z*)-**1** (5.6 mM in $CDCl_3$) or (B) TFA (0-40 equiv., 1.18 M in $CDCl_3$) to (*Z*)-**1** (6.7 mM in $CDCl_3$). Signals H_g and H_f (See Figure 3 for assignment) are colored to highlight the inversion in chemical shift that occurs at higher equivalents of TFA.

When a solution containing excess TFA (32 equiv.) was then left to equilibrate, the ^{1}H NMR signals for the protonated species (*Z*)-**1**·H$^+$ disappeared and a new set of signals emerged (Figure 3). A NOE-diff. experiment revealed a through-space interaction between the olefinic proton (H_f) and the 3-oxindole NH-proton (H_e) (Figure E4), supporting formation of the *E*-isomer. Furthermore, the NOESY spectrum of (*E*)-**1**·**H**$^+$ indicated that the olefinic proton (H_f) is in close proximity to an N-heterocyclic proton (H_j), while no coupling was observed with the pyridinium proton (H_k) (Figure E5). Very likely, hydrogen bonding between the pyridinium and carbonyl group leads to a fixed orientation of the N-heterocycle as was predicted by DFT calculations. Remarkably, within a day, nearly quantitative isomerization to the *E*-isomer was observed, i.e., a mixture enriched to 95% in (*E*)-**1**·H$^+$ was obtained at thermal equilibrium (Figure 3, Figure E3).

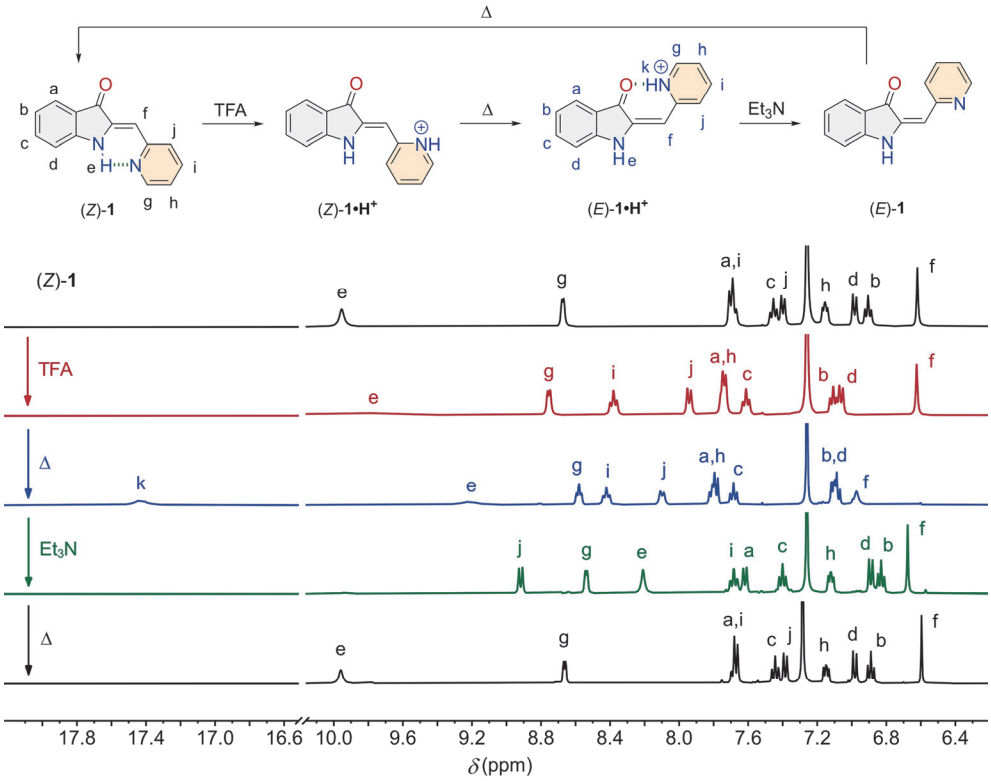

Figure 3. Selected regions in the ^{1}H NMR spectrum (400 MHz) of (*Z*)-**1** (5.7 mM in $CDCl_3$) before and after addition of TFA (32 equiv.) to give (*Z*)-**1**·H$^+$, followed by flame-sealing of the NMR tube and thermal equilibration at rt for 3 days to afford (*E*)-**1**·H$^+$, opening of the NMR tube with a diamond glass file and addition of Et_3N (48 equiv.) to give (*E*)-**1**, and flame-sealing of the NMR tube and thermal equilibration at rt for 9 days to reobtain (*Z*)-**1**.

When the amount of TFA was lowered, however, the *E*/*Z* ratio decreased (Figures E1-E3), even while protonation of **1** was established. A possible explanation was sought in pyridinium-trifluoroacetate ion-pair formation, which can compete with the stabilizing intramolecular hydrogen bond formation. This ion-pair is proposed to be solvated in the presence of larger amounts of TFA,[33,34] explaining the difference in conversion to the *E*-isomer. Furthermore, increasing the amount of TFA accelerated isomerization (Figures E17-E18), hinting at an acid-catalyzed process. A similar observation was made previously for other conjugated olefins, including stilbene derivatives[35-37] and diaryl-hemiindigos.[38]

Interestingly, the *Z*-isomer could be regained by basification of the solution. When Et_3N was added (48 equiv.) to an equilibrated sample of **1** in the presence of TFA (32 equiv.), most pyridyl proton signals now shifted back upfield (H_g, H_h, H_i, Figure 3), indicative of deprotonation. Over the course of several days, (*E*)-**1** fully isomerized back to (*Z*)-**1** (Figure 3, Figure E6), hence completing the thermal acid/base-controlled switching as outlined in Scheme 1A. For hemi-indigos **2**-**6**, the thermal isomerization behavior was comparable (Table 1, Figures E7-E16). The dimethylamino- and bromo-substituted pyridyl derivatives **2** and **3**, as well as the quinolyl derivative **4**, showed identically high conversion to the *E*-isomer when protonated (>95%), while differences in isomerization rates among the different compounds were small (Table 1). For imidazole-based derivatives **5** and **6**, conversion to the *E*-isomer was lower (85% and 88%, respectively), and while the former compound exhibited the slowest isomerization in the series, this process was the fastest for the latter. After neutralization of the solution by Et_3N addition, all compounds displayed quantitative isomerization back to their *Z* isomer, and in this case, large variations were observed in the *E*-to-*Z* isomerization rate. It is worth noting that for the structurally related hemi-thioindigo, Hammett analysis indicated that electron-donating *para*-substituents can lower the thermal isomerization barrier, most likely because of the increase in donor-acceptor character.[39] To summarize, the choice of N-heterocyclic ring can thus be used to tune the thermal isomerization rates.

Table 1. Thermal isomerization parameters upon protonation and subsequent deprotonation.[a]

Hemi-indigo	Ratio [*E*/*Z*·H$^+$][b]	$k_{ZH \rightarrow EH}$ [min^{-1}][c]	$k_{E \rightarrow Z}$ [min^{-1}][c]
1	95:5	4.73×10^{-3}	7.43×10^{-4}
2	>95:5	2.34×10^{-3}	4.83×10^{-3}
3	>95:5	3.05×10^{-3}	2.50×10^{-4}
4	>95:5	4.45×10^{-3}	2.31×10^{-1}
5	85:15	1.56×10^{-3}	3.10×10^{-2}
6	88:12	2.54×10^{-2}	2.42×10^{-4}

[a] Determined by ^{1}H NMR spectroscopy at 25 °C using ~6 mM solutions in $CDCl_3$ containing 32 equiv. of TFA, which were neutralized by subsequent addition of 48 equiv. of Et_3N. [b] Calculated by ^{1}H NMR signal integration. [c] Calculated by fitting to a first order decay.

Protonation and thermal *E*/*Z* isomerization were accompanied by distinct color changes and were additionally monitored using UV-vis spectroscopy (Figure 4A-B, Figures E19-E24). All compounds absorbed in the visible region, characterized by absorption maxima between 478–508 nm. In the case of pyridyl derivative (*Z*)-**1**, addition of TFA was accompanied by a large bathochromic shift (λ_{max} = 482 to 504 nm). When the solution was allowed to equilibrate, the absorption shifted to longer wavelength (λ_{max} = 549 nm) and decreased in intensity (Figure 4B, Figure E19). This red-shifted absorption is in agreement with time-dependent DFT calculations for (*Z*)-**1**·H$^+$ (λ_{max} = 505 nm) and (*E*)-**1**·H$^+$ (λ_{max} = 554 nm) and thus, supportive of *Z*-to-*E* isomerization (Figure E35). Subsequent addition of excess Et_3N to basify the solution led to a hypsochromic shift (λ_{max} = 489 nm), and over time, the original UV-vis spectrum was recovered, demonstrating reversibility of the protonation-induced isomerization.

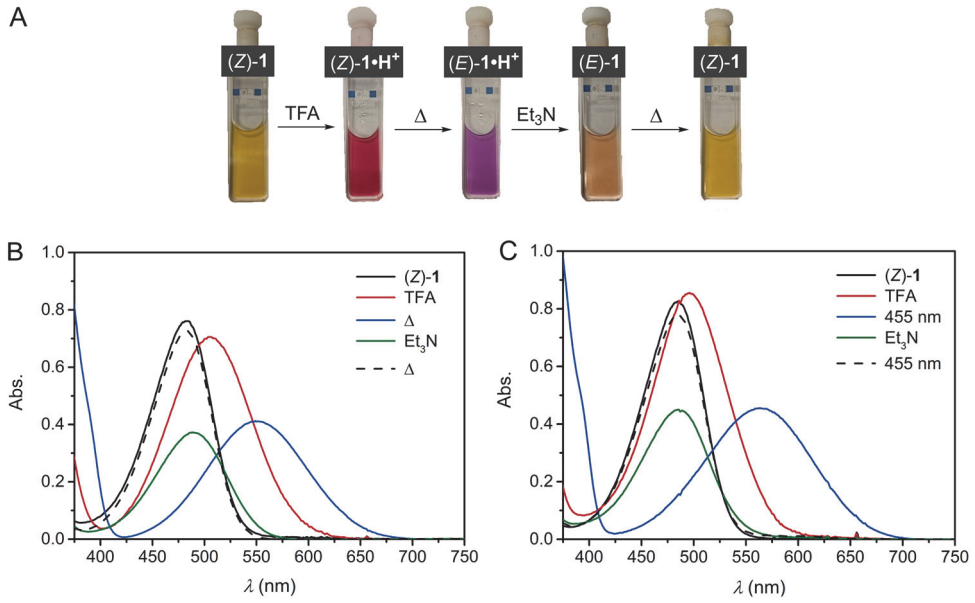

Figure 4. (A) Naked-eye color changes corresponding to the UV-vis thermal equilibration experiments. (B) UV-vis spectral changes starting with a solution of (*Z*)-**1** (0.76 mM in degassed $CHCl_3$, 1 mm quartz cuvette) before and after addition of excess TFA (4.3×10^2 equiv.), followed by equilibration at rt for 15 h, treatment with Et_3N (1.6 equiv. with respect to TFA), and equilibration at rt for 24 h. Please note that direct addition of TFA and Et_3N to the same solution of (*Z*)-**1** also results in a slight decrease in molar absorptivity as is observed here after the full switching cycle has been completed (Figure E19). (C) UV-vis spectra starting with (*Z*)-**1** (0.076 mM in degassed $CHCl_3$, 1 cm quartz cuvette), addition of TFA (5.5 µL, 4.7×10^2 equiv.), irradiation with 455 nm, addition of Et_3N (15 µL, 7.0×10^2 equiv.) and irradiation with 455 nm to recover the original UV-vis absorption spectrum of (*Z*)-**1**.

For hemi-indigos **2**-**4**, similar shifts were observed upon TFA addition, whereas the imidazole-based derivatives **5** and **6** mainly showed a decrease in absorptivity with only a minimal change in absorption maximum (Figures E20-E24). Nevertheless, in all cases, *Z*-to-*E* isomerization was accompanied by a large bathochromic shift, and clear isosbestic points were observed.

2.5 Monodirectional Photoisomerization Cycle

After having identified the UV-vis absorbance and ^{1}H NMR signatures of all neutral and protonated isomers, we set out to investigate the photoisomerization behavior. It is important to note that UV-vis irradiation studies were performed at lower temperature (≤ 0 °C) than the isomerization experiments described above to suppress the thermally activated process. In line with reported data,[24,25] exposure of a solution of (*Z*)-**1** to various wavelengths of light did not cause any UV-vis spectral changes (Figure E25), which confirms that photochemical isomerization is inhibited. To our delight, after the addition of TFA, irradiation at 455 nm afforded a bathochromically shifted absorbance profile similar to the one observed for the thermally generated (*E*)-**1**·H$^+$ species (Figures 4C-5), thus revealing that photoisomerization can occur in the protonated state. Likewise, in the ^{1}H NMR spectrum, the same set of signals that was observed upon acid-induced thermal isomerization appeared after irradiation of a solution of the *Z* isomer in the presence of TFA, further supporting that the *E* isomer can be generated photochemically upon protonation (Figure E32).

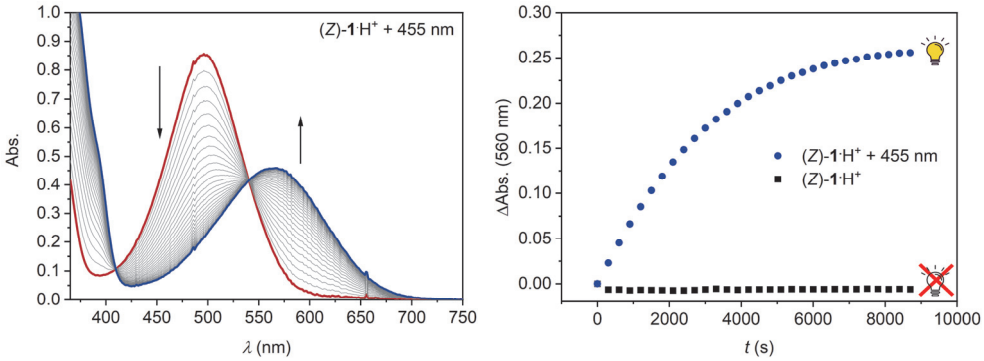

Figure 5. (left) UV-Vis spectral changes of (*Z*)-**1**·H$^+$ upon continuous irradiation at 455 nm, and (right) change in absorbance of (*Z*)-**1**·H$^+$ at 560 nm with and without of irradiation. In the latter case, virtually no change in absorbance was observed, showing that thermal isomerization is negligible under the experimental conditions used (as described in Figure 4C).

Strikingly, when a sample of (*E*)-**1**·H$^+$ (generated using 455 nm light) was subsequently exposed to other wavelengths, including those at which only this protonated isomer and not the (*Z*)-**1**·H$^+$ species absorbs (>625 nm), no spectral changes were noted. This result suggests that backwards photoisomerization is inhibited in the protonated state, potentially due to excited state intramolecular proton transfer (ESIPT), as has been demonstrated for indigo,[40] and was similarly observed for (*Z*)-**1**[24,25] and the *E*-isomer of structurally related indole-derived hemi-thioindigo.[27] Yet, addition of excess Et_3N, which afforded the absorption spectrum characteristic for (*E*)-**1** (Figure 4C), allowed full isomerization back to the original

(*Z*)-**1** upon irradiation at 455 nm (Figure 6). Forward and backward isomerization reactions were thus achieved in respective protonated and neutral forms by using light of the same wavelength, where thermal isomerization was negligible under the experimental conditions used.

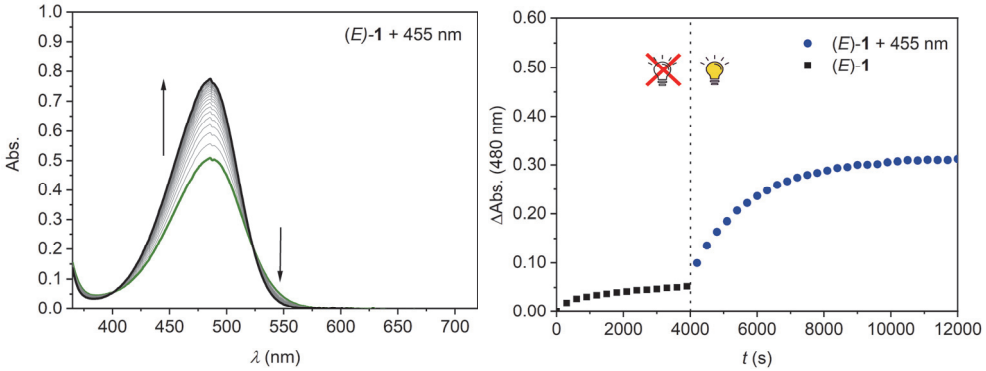

Figure 6. UV-Vis spectral changes of (*E*)-**1** under continuous irradiation at 455 nm, and (right) changes in absorbance of (*E*)-**1** at 480 nm with and without irradiation. In the latter case, minor thermal isomerization is observed under the experimental conditions used (as described in Figure 4C)

The same acid/base-controlled photoresponsivity applied to hemi-indigos **2**-**6** (Figures E26-E31). Interestingly, for dimethylamino-substituted derivative **2**, the entire cycle could be performed using 525 nm instead of 455 nm light owing to its red-shifted absorption (λ_{max} = 511 nm, Table E7 and Figure E26). For (*Z*)-**3**, a larger amount of TFA was required for successful photoconversion (Figure E27), and besides, the generation of (*E*)-**6**·H^+ was limited by the poor photostability of (*Z*)-**6**·H^+ (Figures E30-E31). Nevertheless, when (*E*)-**6**·H^+ was first accessed *via* thermal isomerization, subsequent photoisomerization from (*E*)-**6** to (*Z*)-**6** proceeded smoothly under 455 nm irradiation after Et_3N addition.

The quantum yields for 455 nm induced *Z*-to-*E* isomerization in the protonated state and *E*-to-*Z* isomerization in the neutral state were determined using potassium ferrioxalate as an actinometer. By monitoring the UV-vis absorbance changes upon irradiation of concentrated solutions of *Z* isomer in the presence of excess TFA, the rates of formation of the protonated *E*-isomers were determined. Using the photon flux, the quantum yields were then calculated, which ranged around 1% for compounds **1**-**4**, and were significantly lower for **5** (Table 2). The rates of formation of the neutral *Z*-isomers were determined by first generating the *E*-isomers (by thermal equilibration) in the presence of excess TFA, which was followed by neutralization with Et_3N and 455 nm irradiation. Here, the variation in quantum yield

between the different N-heterocyclic hemi-indigos was larger, with the highest values (≥ 3.5%) found for **2** and **5**, and that of **1** and **3** being about 10 times lower.

Table 2. Photoisomerization quantum yields of hemi-indigos **1**-**5**.[a,b]

Compound[c]	$\Phi_{Z\text{-}H+ \rightarrow E\text{-}H+}$ (%)	$\Phi_{E \rightarrow Z}$ (%)
1	0.76 ± 0.011	0.34 ± 0.003
2	1.23 ± 0.014	3.9 ± 0.035[d]
3	0.85 ± 0.003	0.24 ± 0.010
4	0.88 ± 0.003	n.d.[e]
5	0.20 ± 0.001	3.5 ± 0.099[d]

[a] At 455 nm irradiation in $CHCl_3$ at 273 K, unless otherwise noted. [b] Standard deviations are from duplicate measurements. [c] Not determined for compound **6** because of poor photostability. [d] Determined at 263 K. [e] Not determined because of rapid thermal *E*-to-*Z* isomerization of compound **4**.

These results confirm that *Z*-to-*E* isomerization is enabled in the protonated form, while the reverse isomerization process takes place in the neutral form. To the best of our knowledge, such a feature has not been observed in photoswitchable systems before. It is also fundamentally different from earlier reported examples of acid-gated photoresponsivity,[37,41-43] which allowed both switching directions in at least one of the states. In our case, only a single (and opposite for neutral and protonated forms) direction of photoswitching is suppressed, affording quantitative conversion by default. It leads to a unique monodirectional cycle of interconversion between species under continuous illumination once a protonation equilibrium is established, thereby displacing associated protons in a specific direction.

2.6 Conclusions

In summary, unprecedented photo- and thermal isomerization behavior was discovered for N-heterocyclic hemi-indigos. Disruption and (re-)formation of intramolecular hydrogen bonding interactions were found to be of major importance. It must be recognized that, besides hydrazones,[30] these compounds represent the second family of switches that undergo reversible pH-activated double bond isomerization. More striking, though, is the observed protonation-controlled one-way photoisomerization, giving rise to an exceptional monodirectional interconversion cycle. Unidirectional translocation of associated protons (with respect to the hemi-indigo scaffold) takes place during this cycle. Current efforts in our lab focus on immobilization of these N-heterocyclic hemi-indigos in porous materials and membranes, in addition to time-resolved spectroscopic studies. Furthermore, we envision that the selective inhibition of either forwards or backwards photoisomerization paths by binding of a substrate[44] can be applied as a general approach for directional transport and pumping of that substrate. It is a tantalizing prospect, as it would give the ability to effectively generate concentration gradients in artificial compartmentalized systems using broad-spectrum (solar) light as the energy source.

2.7 Contributions

N. Duindam and S. J. Wezenberg conceived the project. N. Duindam carried out the experimental work with assistance from M. van Dongen. M. A. Siegler performed the XRD measurements. S. J. Wezenberg guided the project.

2.8 Experimental Section

General methods and materials

Toluene was dried using a Pure Solve 400 solvent purification system from Innovative Technology. $CDCl_3$ was purchased from Eurisotop, which was filtered over basic Al_2O_3 (to remove DCl). The degassing of the solvents was carried out by purging with N_2 for 15 min, unless noted otherwise. Aldehydes **8**[45] and **9**[46] were synthesized as describe elsewhere. All other chemicals were commercially available and were used without further purification. Flash chromatography (FC) was performed using silica gel (SiO_2) purchased from Screening Devices BV (60 M, 0.04-0.063 mm). Thin-layer chromatography (TLC) was carried out on aluminum sheets coated with silica 60 F254. Compounds were visualized with UV light (254 nm or 365 nm). ^1H and ^{13}C NMR spectra were recorded on Bruker AV-I-400, Bruker AV-IV 400, Bruker AV-IV- 500 Ultra Shield, and Bruker AV-III-600 instruments at 294 K unless indicated other-wise. Chemical shifts (δ) are denoted in parts per million (ppm) relative to residual protiated solvent ($CDCl_3$: for ^1H detection, $\delta = 7.26$ ppm; for ^{13}C detection, $\delta = 77.16$ ppm). The splitting pattern of peaks is designated as follows: s (singlet), d (doublet), t (triplet), q (quartet), p (quintet), h (septet), m (multiplet), br (broad). High-resolution mass spectrometry (ESI-MS) was performed on a Thermo Scientific Q Exactive HF spectrometer with ESI ionization. IR spectra were recorded on a Perkin Elmer Spectrum Two FT-IR spectrometer. The intensity of bands ($\nu = cm^{-1}$) is assigned as follows: s (strong), m (medium), w (weak), very w (very weak), br (broad), and sh (shoulder). Melting points were determined with a Büchi M560 apparatus. UV-Vis spectra were recorded on an Agilent Cary 8454 spectrometer equipped with a stirrer (250 rpm) and a temperature control unit (293 K unless noted otherwise) using 1 cm or 1 mm quartz cuvettes. A Newport 20CGA–360 KI162 Longpass filter was placed in front of the light source of the spectrophotometer to absorb all incident light below 360 nm. Irradiation of UV-Vis and NMR samples was carried out using LEDs purchased from Thorlabs, i.e. mounted fiber-coupled LEDs M365F1 (3.0 mW), M385FP1 (18 mW), M405F1 (3.0 mW), M455F3 LEDs (17 mW), unmounted epoxy-encased LED465E (20 mW), LED525E (2.5 mW), LED591E (2 mW), LED630E (7.2 mW), and unmounted LED with glass lens LED660L (13 mW).

General procedure for the synthesis of hemi-indigo dyes 1-7

Based on previously reported literature procedures,[23,32] 1*H*-indol-3-yl acetate (50 mg, 0.29 mmol) was suspended in 1.6 mL degassed 1.5 M aqueous NaOH solution (purged with N_2 for 30 min or subjected to 3 freeze-pump-thaw cycles) under Ar atmosphere. The mixture was heated to 100 °C for 15 min, after which the resulting greenish solution was cooled to 0 °C and the respective aldehyde (0.29 mmol) in MeOH (0.3 mL) was added. The reaction mixture was stirred at room temperature for 3–5 days at rt, diluted with 5 mL water, and extracted with EtOAc (3 × 15 mL). The combined organic layers were dried over Na_2SO_4 and concentrated. Purification by flash chromatography (FC) yielded the desired hemi-indigo product.

(*Z*)-2-(pyridin-2-ylmethylene)indolin-3-one [(*Z*)-1]

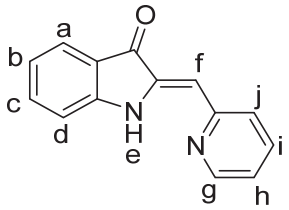

1*H*-indol-3-yl acetate (50 mg, 0.29 mmol) and picolinaldehyde (21 µL, 0.29 mmol) were reacted as described in the general method for 3 days. Purification by FC (SiO_2; EtOAc/pentane 1:18) yielded (*Z*)-**1** as a red solid (43 mg, 68%); R_f = 0.17 (SiO_2; EtOAc/pentane 1:18); m.p. 149.0–151.3 °C ([24]: 153–154 °C); ^{1}H NMR (500 MHz, $CDCl_3$, assignments based on 2D COSY and NOESY spectra) δ = 9.95 (s, 1H; H**e**), 8.67 (d, *J* = 4.9 Hz, 1H; H**g**), 7.71–7.66 (m, 2H; H**a** and H**i**), 7.45 (ddd, *J* = 8.1, 7.2, 1.3 Hz, 1H; H**c**), 7.39 (m, 1H; H**j**), 7.14 (ddd, *J* = 7.5, 4.9, 1.2 Hz, 1H; H**h**), 6.97 (dt, *J* = 8.0, 0.8 Hz, 1H; H**d**), 6.90 (td, *J* = 7.4, 0.8 Hz, 1H; H**b**), 6.61 (s, 1H; H**f**); ^{13}C NMR (126 MHz, $CDCl_3$) δ = 187.9, 156.1, 153.3, 149.4, 138.4, 136.7, 136.6, 126.3, 125.2, 121.6, 120.9, 120.2, 111.7, 105.3; IR (ATR) ν = 3353-3328 (br. w), 2998-2850 (w), 1690 (m), 1629 (w, sh), 1598 (m), 1584 (m), 1482 (m),1460 (m), 1437 (m), 1380 (m), 1358 (w, sh), 1275 (m), 1261 (w, sh), 887 (w), 850 (w), 763 (s, sh), 747 (very s); HRMS (ESI) *m/z:* 223.0864 ([M+H]$^+$, calcd for $C_{14}H_{11}N_2O^+$: 223.0866). The spectroscopic data is in agreement with the literature.[24]

(*Z*)-2-{[5-(dimethylamino)pyridin-2-yl]methylene}indolin-3-one [(*Z*)-2]

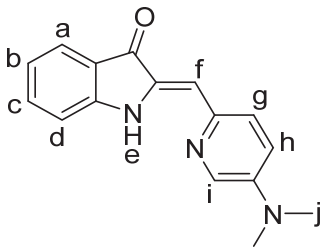

1*H*-indol-3-yl acetate (50 mg, 0.29 mmol) was reacted with 5-(dimethylamino)picolinaldehyde (45 mg, 0.29 mmol) as described in the general procedure for 5 days, with the exception that CH_2Cl_2 was used in the extraction. Purification by FC (SiO_2; CH_2Cl_2 to EtOAc/CH_2Cl_2 1:9) yielded (*Z*)-**2** as a dark-red crystalline solid (54 mg, 72%); R_f = 0.54 (SiO_2; EtOAc/CH_2Cl_2 1:9); m.p. 258.9–261.2 °C; ^{1}H NMR (500 MHz, $CDCl_3$, assignments based on 2D COSY and NOESY spectra) δ = 9.76 (s, 1H; H**e**), 8.23 (d, *J* = 3.1 Hz, 1H; H**i),** 7.70 (d, *J* = 7.7 Hz, 1H; H**a**), 7.41 (ddd, *J* = 8.2, 7.2, 1.3 Hz, 1H; H**c**), 7.28 (d, *J* = 8.7 Hz, 1H; H**g**), 6.98 – 6.91 (m, 2H; H**d** and H**h),** 6.86 (m, 1H; H**b**), 6.66 (s, 1H; H**f**), 3.06 (s, 6H; H**j);** ^{13}C NMR; (126 MHz, $CDCl_3$) δ = 187.3, 152.8, 144.5, 143.5, 135.9, 135.8, 134.7, 127.3, 124.9, 121.3, 119.4, 118.4, 111.5, 107.7, 40.1; IR (ATR) ν = 3294 (br. w), 2992 (w), 2912 (w), 1676 (m), 1623 (m), 1602 (m), 1593 (m), 1565 (m), 1545 (m), 1486 (m), 1466 (w), 1376 (m), 1306 (m), 1280 (s), 1264 (m), 1227 (m), 1148 (m), 1124 (m), 1099 (m), 962 (w), 870 (w), 861 (w), 829 (w), 767.(s, sh), 751 (s), 714 (s), 631 (m); HRMS (ESI) *m/z:* 266.1287 ([M+H]$^+$, calcd for $C_{16}H_{16}N_3O^+$: 266.1288).

(*Z*)-2-[(5-bromopyridin-2-yl)methylene]indolin-3-one [(*Z*)-3]

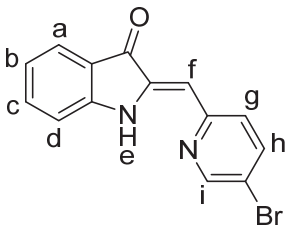

1*H*-indol-3yl acetate (50 mg, 0.29 mmol) was reacted with 5-bromopicolinaldehyde (55 mg, 0.29 mmol) as described in the general procedure for 5 days. Purification by FC (SiO_2; EtOAc/Pet. Ether 0:1 to 2:8) yielded (*Z*)-**3** as a dark red solid (68 mg, 79%); R_f = 0.19 (SiO_2; EtOAc/Pet. Ether 1:9); m.p. 228.9–230.1 °C; ^{1}H NMR (500 MHz, $CDCl_3$, assignments based on 2D COSY and NOESY spectra) δ = 9.65 (s, 1H; H**e**), 8.69 (d, *J* = 2.4 Hz, 1H; H**i**), 7.78 (dd, *J* = 8.4, 2.4 Hz, 1H; H**h**), 7.68 (d, *J* = 7.6, 1H; H**a**), 7.45 (ddd, *J* = 8.5, 7.3, 1.3 Hz, 1H; H**c**), 7.25 (d, *J* = 7.6 Hz, 1H; H**g**), 6.97 (dt, *J* = 8.1, 0.6 Hz, 1H; H**d**), 6.91 (td, *J* = 7.6, 0.8 Hz, 1H; H**b**), 6.52 (s, 1H; H**f**); ^{13}C NMR (126 MHz, $CDCl_3$) δ = 187.7, 154.5, 153.1, 150.5, 139.3, 138.5, 136.7, 127.1, 125.3, 120.8, 120.5, 118.3, 111.7, 103.9; IR (ATR) ν = 3394 (w), 2919 (br. m), 2860 (w), 1693 (m), 1632 (m), 1608 (m), 1591 (sh), 1568 (w), 1486 (m), 1462 (m), 1401 (m), 1355 (m), 1317 (w, sh), 1306 (m), 1290 (m, sh), 1220 (s), 1196 (m, sh), 1162 (w), 1145 (m), 1130 (m), 1088 (br. m), 1009 (m), 966 (w), 873 (m), 861 (m), 851 (m, sh), 829 (m) 757 (w), 712 (m); HRMS (ESI) *m/z:* 300.9971 ($[M+H]^+$, calcd for $C_{14}H_{10}BrN_2O^+$: 300.9971).

(*Z*)-2-(quinolin-2-ylmethylene)indolin-3-one [(*Z*)-4]

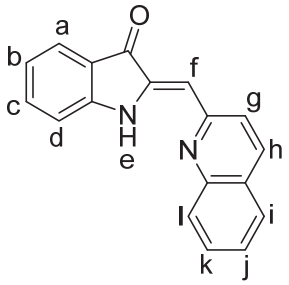

1*H*-indol-3yl acetate (50 mg, 0.29 mmol) was reacted with quinoline-2-carbaldehyde (45 mg, 0.29 mmol) as described in the general procedure for 3 days. Purification by FC (SiO_2; EtOAc/Pet. Ether 1:9) yielded (*Z*)-**4** as a bright red solid (56 mg, 73%); R_f = 0.16 (SiO_2; EtOAc/Pet. Ether 1:9); m.p. 155.1–155.7 °C; ^{1}H NMR; (500 MHz, $CDCl_3$, assignments based on 2D COSY and NOESY spectra) δ = 10.47 (s, 1H; H**e**), 8.11–8.03 (m, 2H; H**l** and H**h**), 7.77 (dd, *J* = 8.2, 1.4 Hz, 1H; H**i**), 7.74–7.68 (m, 2H; H**a** and H**k**), 7.49 (m, 2H; H**c** and H**j**), 7.44 (d, *J* = 8.5 Hz, 1H; H**g**), 7.02 (dt, *J* = 8.0, 0.8 Hz, 1H; H**d**), 6.93 (td, *J* = 7.4, 0.8 Hz, 1H; H**b**), 6.70 (s, 1H; H**f**); ^{13}C NMR; (126 MHz, $CDCl_3$) δ = 188.0, 156.4, 153.3, 148.1, 139.3, 136.7, 136.4, 130.1, 128.9, 127.8, 126.7 (2), 125.3, 124.2, 120.9, 120.5, 111.8, 104.7; IR (ATR) ν = 3326 (br. w), 3058 (w), 2927 (w), 2857 (w), 1702 (m, sh), 1691 (m), 1640 (m), 1622 (m), 1590 (s), 1487 (m), 1470 (br. m), 1402 (m), 1374 (m), 1314 (m), 1291 (w), 1219 (m), 1204 (m, sh), 1137 (m), 1119 (w), 1097 (w), 849 (m), 820 (m), 754 (w), 740 (m), 709 (m), 617 (w); HRMS (ESI) *m/z*: 273.1020 ([M+H]$^+$, calcd for $C_{18}H_{13}N_2O^+$: 273.1022).

(*Z*)-2-[(1-methyl-1*H*-imidazol-2-yl)methylene]indolin-3-one [(*Z*)-5]

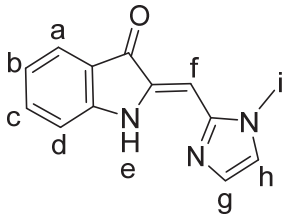

1*H*-indol-3-yl acetate (50 mg, 0.29 mmol) and 1-methyl-1*H*-imidazole-2-carbaldehyde (31 mg, 0.29 mmol) were reacted as described in the general procedure for 3 days. Purification by FC (SiO_2; EtOAc/pentane 2:3) yielded (*Z*)-**5** as an orange solid (53 mg, 82%); R_f = 0.32 (SiO_2; EtOAc/pentane 2:3); m.p. 201.1–202.3 °C; ^{1}H NMR; (500 MHz, $CDCl_3$, assignments based on 2D COSY and NOESY spectra) δ = 9.59 (s, 1H; H**e**), 7.68 (d, *J* = 7.6 Hz, 1H; H**a**), 7.43 (ddd, *J* = 8.1, 7.2, 1.3 Hz, 1H; H**c**), 7.23 (d, *J* = 1.1 Hz, 1H; H**g**), 6.96 (dt, *J* = 8.1, 0.8 Hz, 1H; H**d**), 6.94 (d, *J* = 1.2 Hz, 1H; H**h**), 6.89 (ddd, *J* = 7.8, 7.3, 0.8 Hz, 1H; H**b**), 6.51 (d, *J* = 0.5 Hz, 1H; H**f**), 3.75 (s, 3H; **i**); ^{13}C NMR (126 MHz, $CDCl_3$) δ = 187.1, 153.6, 146.0, 137.4, 136.4, 130.1, 125.1, 122.3, 121.3, 120.1, 111.8, 92.2, 33.1; IR (ATR) ν = 3325 (m), 3132 (w), 3115 (w), 2929 (br. m), 2858 (m), 1687 (m), 1627 (m), 1586 (s), 1476 (m), 1445 (m), 1350 (m), 1312 (m), 1292 (m, sh), 1281 (s), 1263(m, sh), 1223 (m), 1192 (m), 1174 (m), 1145 (m), 1119 (m), 1097 (m), 1081 (m), 1046 (m), 968 (w), 927 (w), 890 (w), 831 (w), 792 (m), 752 (s), 722 (m), 709 (m), 677 (w), 624 (w); HRMS (ESI) *m/z:* 226.0972 ([M+H]$^+$, calcd for $C_{13}H_{12}N_3O^+$: 226.0975).

(*Z*)-2-[(1-methyl-1*H*-imidazol-4-yl)methylene]indolin-3-one [(*Z*)-6]

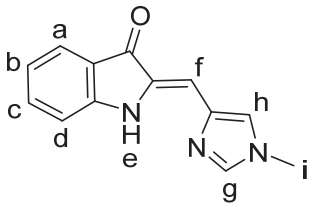

1*H*-indol-3-yl acetate (50 mg, 0.29 mmol) was reacted with aldehyde **8** (40 mg, 0.36 mmol) as described in the general procedure for 3 days. Purification by FC (SiO_2; EtOAc/pentane 2:3 to EtOAc/pentane 4:1) yielded (*Z*)-**6** as a yellow solid (42 mg, 65%); R_f = 0.15 (SiO_2; EtOAc/ pentane 3:2); m.p. 166.4–166.7 °C; ^{1}H NMR (500 MHz, $CDCl_3$, assignments based on 2D COSY and NOESY spectra) δ = 9.14 (s, 1H; H**e**), 7.68 (d, J = 7.7 Hz, 1H; H**a**), 7.51 (s, 1H; H**g**), 7.40 (ddd, J = 8.3, 7.2, 1.3 Hz, 1H; H**c**), 7.12 (d, J = 0.9 Hz, 1H; H**h**), 6.94 (dt, J = 8.1, 0.9 Hz, 1H; H**d**), 6.84 (ddd, J = 7.8, 7.2, 0.8 Hz, 1H; H**b**), 6.65 (s, 1H; H**f**), 3.72 (s, 3H; H**i**); ^{13}C NMR (126 MHz, $CDCl_3$) δ = 186.8, 152.7, 139.5, 138.7, 135.8, 135.4, 124.8, 122.8, 121.4, 119.2, 111.5, 101.6, 33.8; IR (ATR) ν = 3352 (m), 3129 (w), 2997 (m), 2921 (m), 1687 (m), 1637 (m), 1606 (m), 1588 (m, sh), 1547 (m), 1484 (m), 1465 (m), 1377 (m), 1334 (m), 1312 (m), 1280 (m), 1264 (m), 1241 (m), 1129 (m), 1098 (m), 988 (w), 824 (w), 768.40 (s, sh) 755 (s), 753.64 (s), 740 (s, sh), 704 (m), 614 (m); HRMS (ESI) *m/z:* 226.0972 ([M+H]$^+$, calcd for $C_{13}H_{12}N_3O^+$: 226.0975).

(*Z*)-2-benzylideneindolin-3-one [(*Z*)-7]

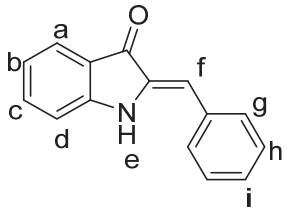

1*H*-indol-3-yl acetate (50 mg, 0.29 mmol) was reacted with benzaldehyde (29 µL, 0.29 mmol) as described in the general procedure for 3 days. Purification by FC (SiO_2; EtOAc/Pet. Ether 1:5) yielded **7** as a red solid (58 mg, 92%); ^{1}H NMR (500 MHz, $CDCl_3$, assignments based on 2D COSY and NOESY spectra) δ = 7.76 (d, J = 7.7 Hz, 1H, H**a**), 7.56 (d, J = 7.4 Hz, 2H, **g**), 7.52 – 7.42 (m, 3H, H**c** and H**h**), 7.38–7.30 (m, 1H, H**i**), 7.02–6.95 (m, 1H, H**b** and H**d**), 6.88 (s, 1H, H**f**), 6.82 (s, 1H, H**e**); ^{13}C NMR (126 MHz, $CDCl_3$) δ = 186.7, 153.3, 136.3, 135.5, 134.9, 129.6, 129.4, 128.7, 125.2, 122.0, 120.9, 112.1, 111.7. Spectral data are in accordance with the literature,[47] except for the chemical shift of H**e** (δ = 6.82 ppm versus 7.05 ppm), which presumably is dependent on concentration (5.4 mM in our case) and water content.

Crystal Structures

Crystal structures can be accessed on www.ccdc.cam.ac.uk/data_request/cif under CCDC codes 2234394-2234398.

Table E1. Central double bond length, dihedral angle, and shortest nitrogen-nitrogen distance in the solid-state structures of (*Z*)-**1**-**3** and (*Z*)-**5**-**6** including estimated standard deviations.

Hemi-indigo	N-C=C-C_{Ar} dihedral [°]	C=C bond length [Å]	N(H)···N distance [Å]
(*Z*)-**1**	-1.7(2)[a]	1.3453(16)[a]	2.8212(14)[a]
(*Z*)-**2**	-2.3(2)	1.3545(18)	2.7211(15)
(*Z*)-**3**	1.7(3)	1.346(2)	2.8568(19)
(*Z*)-**5**	0.4(3)	1.350(2)	2.8008(19)
(*Z*)-**6**	-0.6(3)	1.344(3)	2.830(2)

[a] For comparison: in the DFT-optimized structure of (*Z*)-**1** this dihedral angle is 0.0°, and the C=C bond length and N-N distance are 1.353 Å and 2.81 Å, respectively.

Table E2. Crystallographic data for the structure of (*Z*)-**1**.

	(*Z*)-**1**
Crystal data	
Chemical formula	$C_{14}H_{10}N_2O$
M_r	222.24
Crystal system, space group	Monoclinic, $P2_1/n$
Temperature (K)	110
a, *b*, *c* (Å)	7.0582 (2), 14.0070 (4), 10.7964 (4)
β (°)	101.108 (3)
V (Å^3)	1047.38 (6)
Z	4
Radiation type	Mo $K\alpha$
μ (mm^{-1})	0.09
Crystal size (mm)	0.48 × 0.37 × 0.34
Data collection	
Diffractometer	SuperNova, Dual, Cu at zero, Atlas
Absorption correction	Gaussian *CrysAlis PRO* 1.171.41.93a (Rigaku Oxford Diffraction, 2020) Numerical absorption correction based on gaussian integration over a multifaceted crystal model Empirical absorption correction using spherical harmonics, implemented in SCALE3 ABSPACK scaling algorithm.
T_{min}, T_{max}	0.241, 1.000
No. of measured, independent and observed [$I > 2\ \sigma\ (I)$] reflections	19717, 2396, 2187
R_{int}	0.030
$((\sin\theta/\lambda)_{max}$ (Å^{-1})	0.650
Refinement	
$R[F^2 > 2\sigma(F^2)]$, $wR(F^2)$, S	0.037, 0.100, 1.05
No. of reflections	2396
No. of parameters	159
H-atom treatment	H atoms treated by a mixture of independent and constrained refinement
$\Delta\rho_{max}$, $\Delta\rho_{min}$ (e Å^{-3})	0.37, -0.20

Table E3. Crystallographic data for the structure of (*Z*)-**2**.

	(*Z*)-**2**
Crystal data	
Chemical formula	$C_{16}H_{15}N_3O$
M_r	265.31
Crystal system, space group	Monoclinic, $P2_1/n$
Temperature (K)	110
a, b, c (Å)	10.1732 (5), 12.9706 (5), 10.5863 (5)
β (°)	111.973 (6)
V (Å^3)	1295.42 (11)
Z	4
Radiation type	Mo $K\alpha$
μ (mm^{-1})	0.09
Crystal size (mm)	0.23 × 0.20 × 0.06
Data collection	
Diffractometer	SuperNova, Dual, Cu at zero, Atlas
Absorption correction	Gaussian *CrysAlis PRO* 1.171.41.93a (Rigaku Oxford Diffraction, 2020) Numerical absorption correction based on gaussian integration over a multifaceted crystal model Empirical absorption correction using spherical harmonics, implemented in SCALE3 ABSPACK scaling algorithm.
T_{min}, T_{max}	0.666, 1.000
No. of measured, independent and observed [$I > 2\sigma(I)$] reflections	18366, 2980, 2502
R_{int}	0.031
$(\sin \theta/\lambda)_{max}$ (Å^{-1})	0.650
Refinement	
$R[F^2 > 2\sigma(F^2)]$, $wR(F^2)$, S	0.041, 0.108, 1.05
No. of reflections	2980
No. of parameters	187
H-atom treatment	H atoms treated by a mixture of independent and constrained refinement
$\Delta\rho_{max}$, $\Delta\rho_{min}$ (e Å^{-3})	0.29, -0.24

Table E4. Crystallographic data for the structure of (*Z*)-**3**.

	(*Z*)-**3**
Crystal data	
Chemical formula	$C_{14}H_9BrN_2O$
M_r	301.14
Crystal system, space group	Monoclinic, $P2_1/n$
Temperature (K)	110
a, b, c (Å)	6.4263 (2), 10.0678 (3), 18.4821 (6)
β (°)	99.928 (3)
V (Å^3)	1177.86 (6)
Z	4
Radiation type	Mo $K\alpha$
μ (mm^{-1})	3.48
Crystal size (mm)	0.35 × 0.25 × 0.24
Data collection	
Diffractometer	SuperNova, Dual, Cu at zero, Atlas
Absorption correction	Gaussian *CrysAlis PRO* 1.171.41.93a (Rigaku Oxford Diffraction, 2020) Numerical absorption correction based on gaussian integration over a multifaceted crystal model Empirical absorption correction using spherical harmonics, implemented in SCALE3 ABSPACK scaling algorithm.
T_{min}, T_{max}	0.474, 0.908
No. of measured, independent and observed [$I > 2\sigma(I)$] reflections	21070, 2710, 2506
R_{int}	0.031
$(\sin \theta/\lambda)_{max}$ (Å^{-1})	0.650
Refinement	
$R[F^2 > 2\sigma(F^2)]$, $wR(F^2)$, S	0.021, 0.054, 1.05
No. of reflections	2710
No. of parameters	166
No. of restraints	1
H-atom treatment	H atoms treated by a mixture of independent and constrained refinement
$\Delta\rho_{max}$, $\Delta\rho_{min}$ (e Å^{-3})	0.38, -0.31

Table E5. Crystallographic data for the structure of (*Z*)-**5**.

	(*Z*)-**5**
Crystal data	
Chemical formula	$C_{13}H_{11}N_3O$
M_r	225.25
Crystal system, space group	Monoclinic, $P2_1/c$
Temperature (K)	110
a, b, c (Å)	12.6840 (8), 7.9316 (3), 12.0346 (8)
β (°)	116.692 (8)
V (Å^3)	1081.71 (13)
Z	4
Radiation type	Mo $K\alpha$
μ (mm^{-1})	0.09
Crystal size (mm)	0.18 × 0.14 × 0.10
Data collection	
Diffractometer	SuperNova, Dual, Cu at zero, Atlas
Absorption correction	Gaussian *CrysAlis PRO* 1.171.42.49 (Rigaku Oxford Diffraction, 2022) Numerical absorption correction based on gaussian integration over a multifaceted crystal model Empirical absorption correction using spherical harmonics, implemented in SCALE3 ABSPACK scaling algorithm.
T_{min}, T_{max}	0.900, 1.000
No. of measured, independent and observed [$I > 2\sigma(I)$] reflections	12731, 3586, 2227
R_{int}	0.042
$(\sin \theta/\lambda)_{max}$ (Å^{-1})	0.650
Refinement	
$R[F^2 > 2\sigma(F^2)]$, $wR(F^2)$, S	0.039, 0.088, 0.83
No. of reflections	3586
No. of parameters	160
H-atom treatment	H atoms treated by a mixture of independent and constrained refinement
$\Delta\rho_{max}$, $\Delta\rho_{min}$ (e Å^{-3})	0.26, -0.21

Table E6. Crystallographic data for the structure of (*Z*)-**6**.

	(*Z*)-**6**
Crystal data	
Chemical formula	$C_{13}H_{11}N_3O$
M_r	225.25
Crystal system, space group	Monoclinic, *I*2/*a*
Temperature (K)	110
a, *b*, *c* (Å)	20.5498 (14), 3.8316 (3), 27.2403 (18)
β (°)	103.238 (7)
V (Å^3)	2087.9 (3)
Z	8
Radiation type	Mo *K*α
μ (mm^{-1})	0.10
Crystal size (mm)	0.14 × 0.07 × 0.06
Data collection	
Diffractometer	SuperNova, Dual, Cu at zero, Atlas
Absorption correction	Gaussian *CrysAlis PRO* 1.171.42.49 (Rigaku Oxford Diffraction, 2022) Numerical absorption correction based on gaussian integration over a multifaceted crystal model Empirical absorption correction using spherical harmonics, implemented in SCALE3 ABSPACK scaling algorithm.
T_{min}, T_{max}	0.855, 1.000
No. of measured, independent and observed [$I > 2\sigma(I)$] reflections	11387, 2046, 1632
R_{int}	0.056
$(\sin \theta/\lambda)_{max}$ (Å^{-1})	0.617
Refinement	
$R[F^2 > 2\sigma(F^2)]$, $wR(F^2)$, S	0.045, 0.113, 1.08
No. of reflections	2046
No. of parameters	159
H-atom treatment	H atoms treated by a mixture of independent and constrained refinement
$\Delta\rho_{max}$, $\Delta\rho_{min}$ (e Å^{-3})	0.19, -0.25

^{1}H NMR Studies of Acid/Base Controlled Isomerization

Acid-induced *Z*→*E* isomerization

The desired amount of TFA was added to solutions of hemi-indigos **1**-**6** (5.7-5.8 mM in $CDCl_3$, 0.60 mL), and directly after addition, a ^{1}H NMR spectrum was recorded (defined as *t* = 0). Partial isomerization was sometimes observed already at this point due to the exothermic protonation event and the inevitable mixing time prior to data acquisition. The generation of $(E)\cdot H^+$ was monitored over time by ^{1}H NMR spectroscopy, and in case thermal equilibration took longer than 12 h, the experiment was performed in a flame-sealed NMR tube to avoid TFA evaporation (as noted in the figure captions). Flame-sealing of the NMR tubes was performed after measuring the first spectrum. $CDCl_3$ was filtered over basic Al_2O_3 and dried over 4 Å molecular sieves. ^{1}H NMR signal assignments are based on 2D COSY and/or NOESY spectra.

Subsequent *E*→Z back isomerization

Thermally equilibrated samples of hemi-indigos **1**-**6** (in the presence of 32 equiv. TFA) were freshly prepared as described above, and subsequently neutralized with Et_3N (1.5 equiv. with respect to TFA). Isomerization was followed over time by ^{1}H NMR spectroscopy. $CDCl_3$ was filtered over basic Al_2O_3 and dried over 4 Å molecular sieves. All experiments were performed with the same batch of solvent, TFA, and Et_3N. Samples were sonicated before each measurement to ensure homogeneity.

Acid-induced *Z*→*E* isomerization of 1

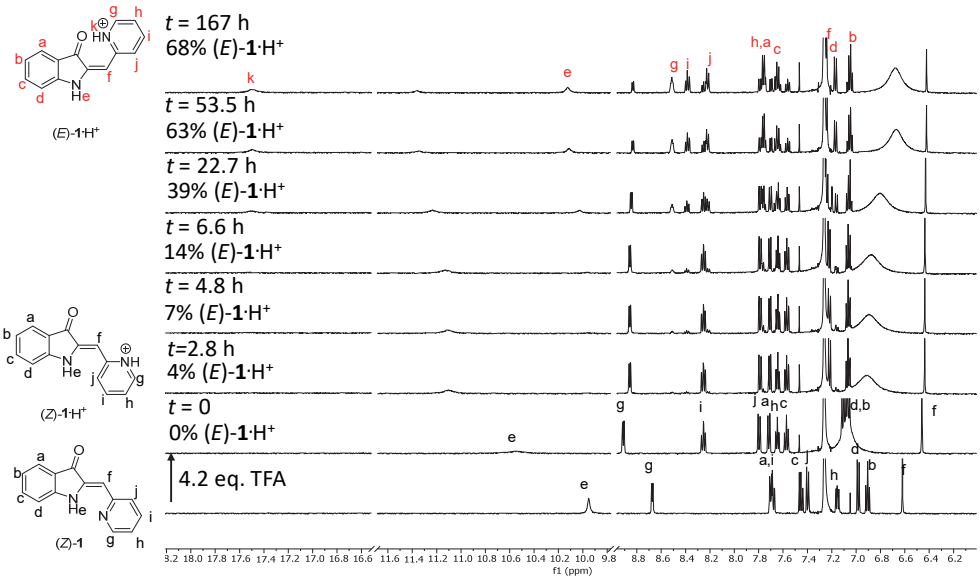

Figure E1. ^{1}H NMR spectral changes (500 MHz, $CDCl_3$) of (*Z*)-**1** (5.7 mM) followed over time (from bottom to top) in a flame-sealed NMR tube after addition of 4.2 equiv. of neat TFA. The isomer ratio was determined by integration of the aromatic H**g** signals.

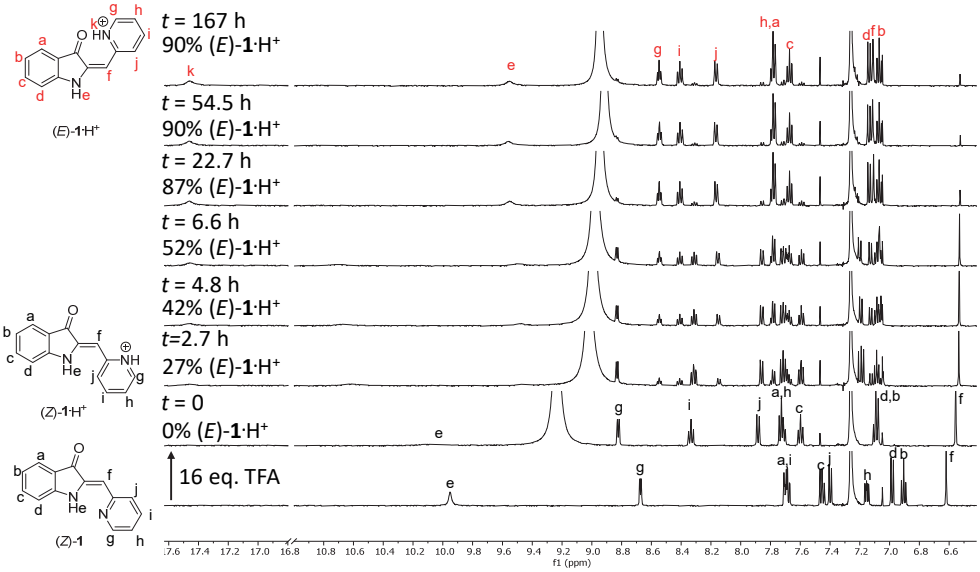

Figure E2. ^{1}H NMR spectral changes (500 MHz, $CDCl_3$) of (*Z*)-**1** (5.7 mM) followed over time (from bottom to top) in a flame-sealed NMR tube after addition of 16 equiv. of neat TFA. The isomer ratio was determined by integration of the aromatic H**i** signals.

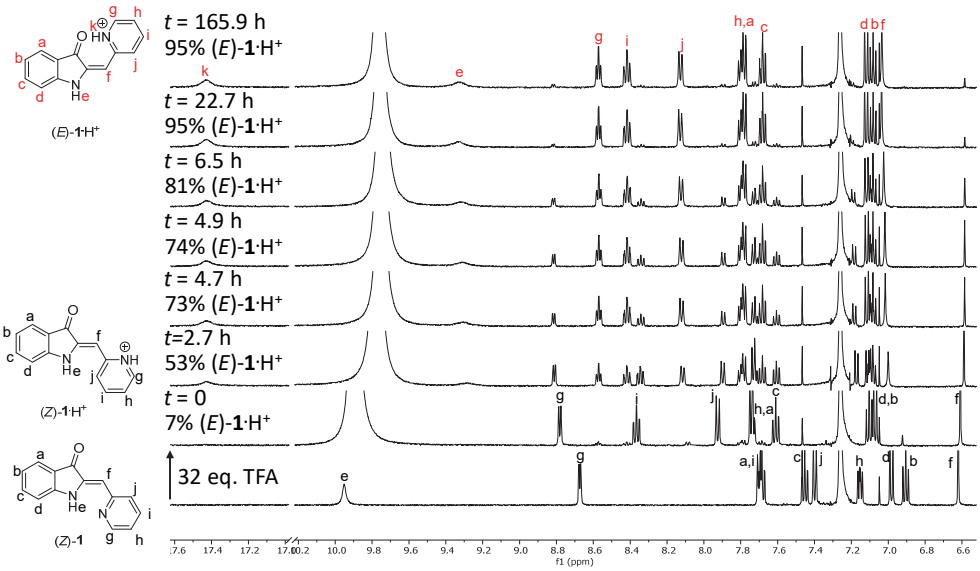

Figure E3. ^{1}H NMR spectral changes (500 MHz, $CDCl_3$) of (*Z*)-**1** (5.7 mM) followed over time (from bottom to top) in a flame-sealed NMR tube after addition of 32 equiv. of neat TFA. The isomer ratio was determined by integration of the aromatic H**g** signals.

2D NOE Interactions

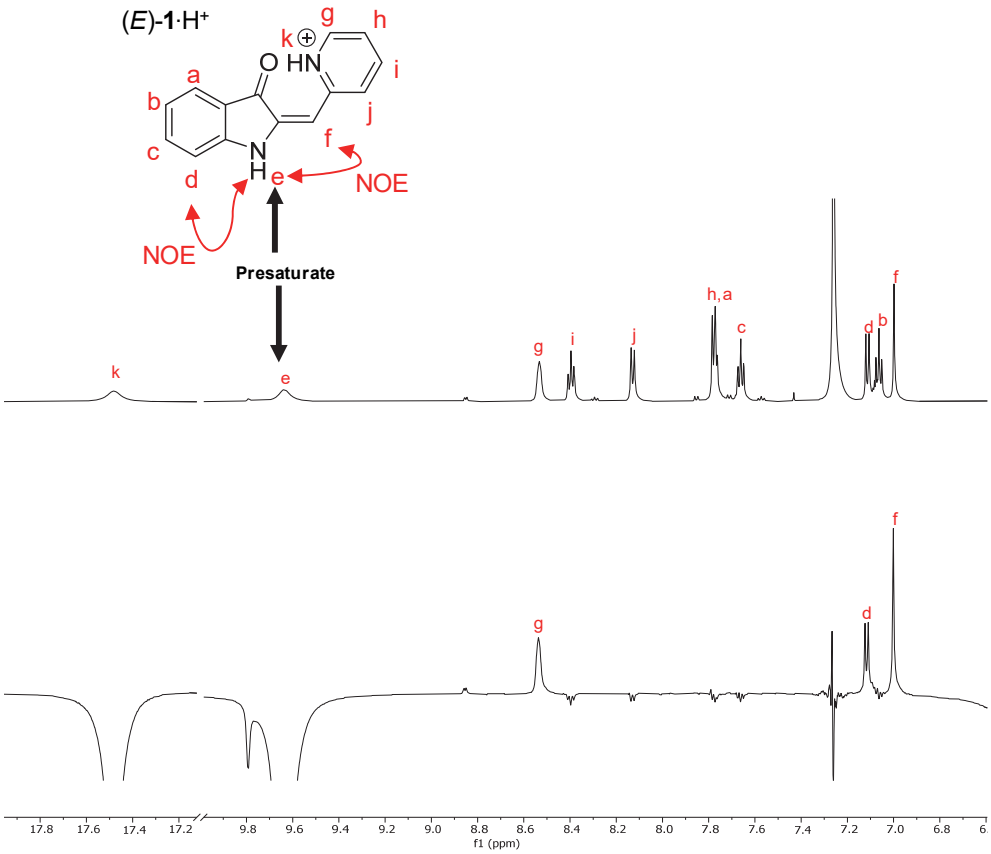

Figure E4. ^{1}H-NMR (600 MHz, $CDCl_3$) (top) and NOE-DIFF NMR (600 MHz, $CDCl_3$) spectrum (bottom) of (*E*)-**1**·**H**$^{+}$ in presence of excess TFA: presaturation pulse at 9.64 ppm; control pulse at 13.06 ppm; pulse length: 3 seconds at 48 dB (1.5849E-5 W). Measured at 298 K. Please note that due to chemical exchange between the acidic protons **k**, **e**, water and TFA presaturation of signal H**e** inevitably leads to presaturation of H**k**. Hence, besides the NOE interaction of H**e** with H**d** and H**f** the NOE interaction between H**k** and H**g** is also observed. Nevertheless, the through-space interaction between H**e** and H**f** supports the (*E*)-configuration of the protonated and thermodynamically more stable form of compound **1**.

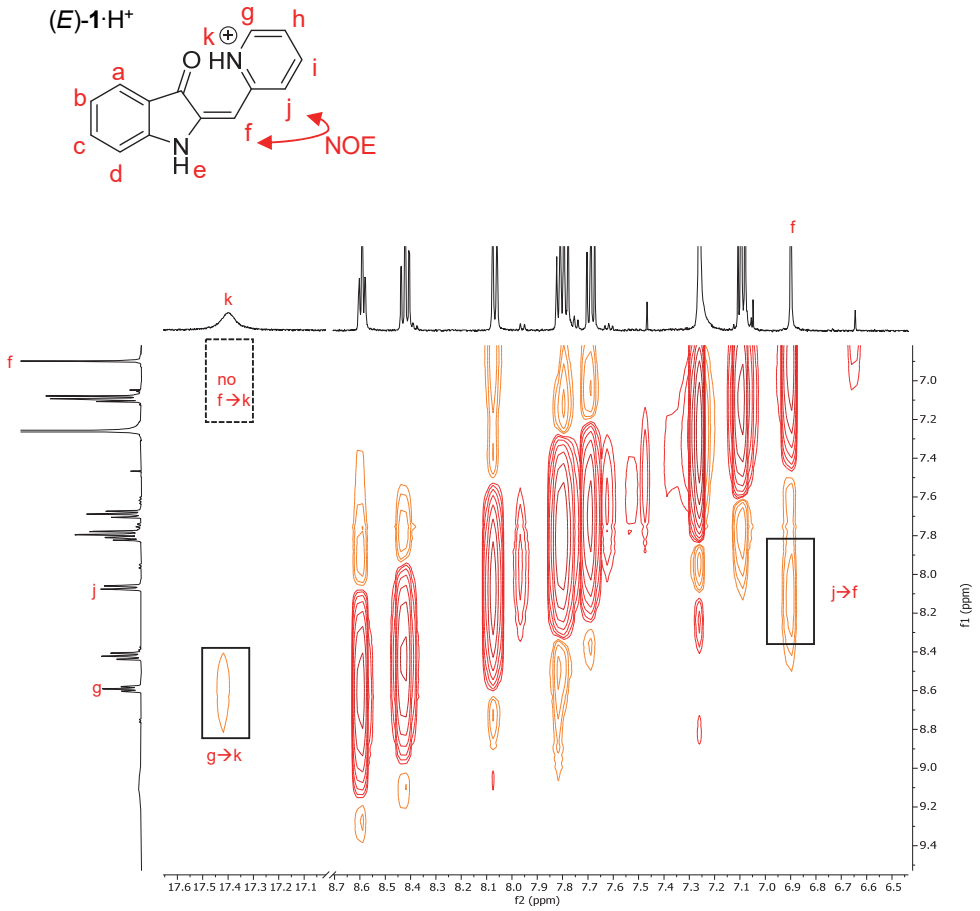

Figure E5. 2D NOESY NMR spectrum (500 MHz, $CDCl_3$) of (*E*)-**1**·**H**$^+$ in presence of excess TFA. The through space interaction between H**j** and H**f** (and the lack of such an interaction between H**k** and H**f**) indicates that the rotational conformer of **1** with the pyridinium proton H**k** oriented towards the carbonyl oxygen is the predominant species in solution.

Subsequent *E*→*Z* back isomerization of 1

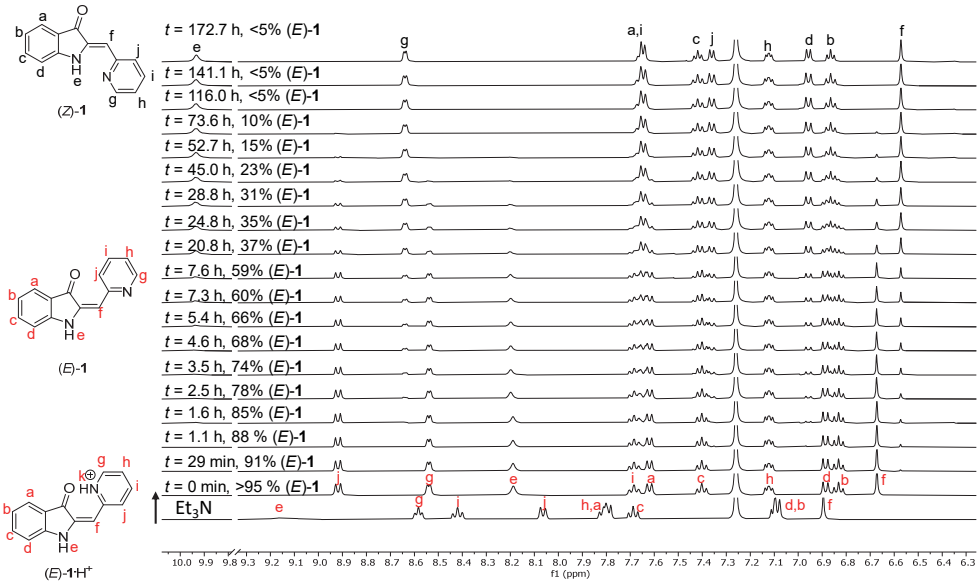

Figure E6. ^{1}H NMR spectral changes (400 and 500 MHz, $CDCl_3$) of (*E*)-**1**·**H**$^+$ (5.7 mM) equilibrated in the presence of 32 equiv. of TFA followed over time (from bottom to top) after addition of 48 equiv. of Et_3N. The isomer ratio was determined by integration of the alkene H**f** signals. Minor precipitation was observed during overnight measurements (between t = 7.6 h and 20.8 h) and sonication was therefore applied to the sample to ensure homogeneity. Note that upon addition of base most pyridyl proton signals shift upfield, indicative of deprotonation. The signal of pyridyl proton H**j**, however, was found to shift downfield. Upon deprotonation, the pyridyl nitrogen will likely rotate away from the carbonyl group, placing this pyridyl proton in close proximity to the anisotropic carbonyl deshielding cone.

Thermal isomerization of 2-5

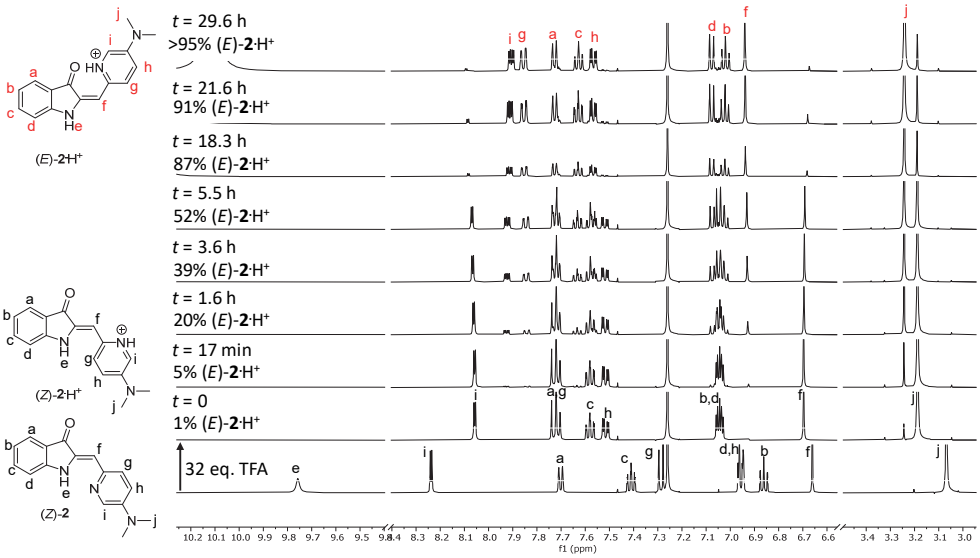

Figure E7. ^{1}H NMR spectral changes (500 MHz, $CDCl_3$) of (*Z*)-**2** (5.8 mM) followed over time (from bottom to top) after addition of 32 equiv. TFA. The isomer ratio was determined by integration of the alkene H**f** signals.

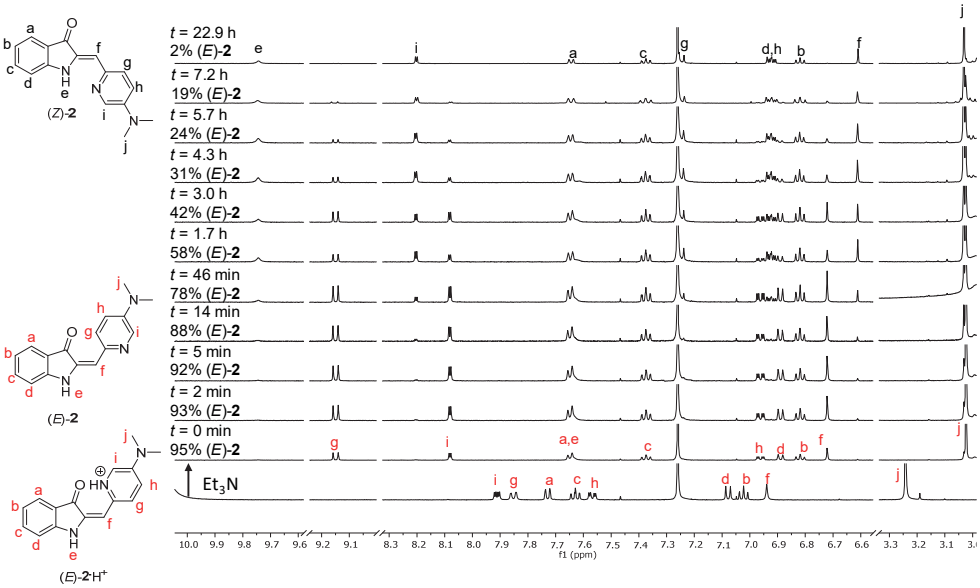

Figure E8. ^{1}H NMR spectral changes (400 MHz, $CDCl_3$) of (*E*)-**2**·**H**$^+$ (5.7 mM) equilibrated in the presence of 32 equiv. TFA followed over time (from bottom to top) after addition of 48 equiv. Et_3N. The isomer ratio was determined by integration of the alkene H**f** signals.

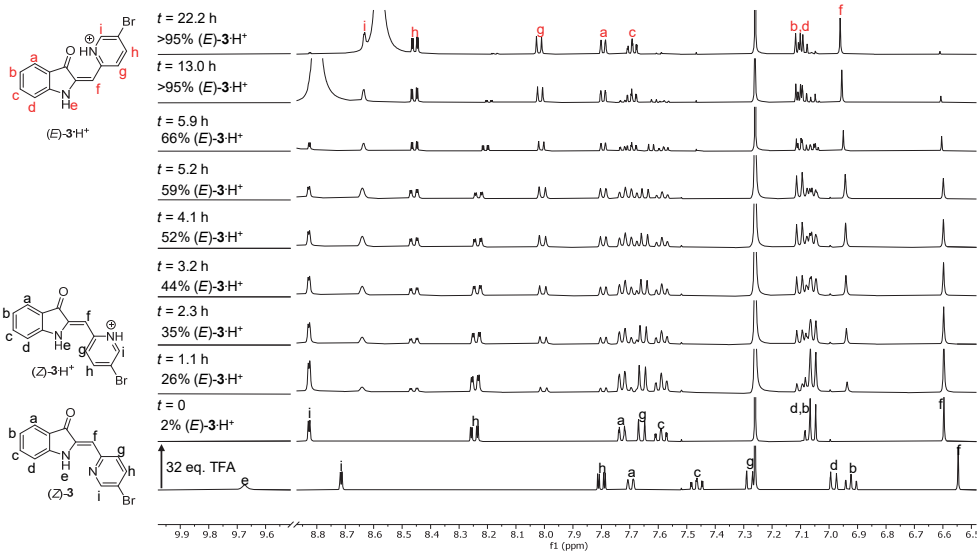

Figure E9. ^{1}H NMR spectral changes (500 MHz, $CDCl_3$) followed over time (from bottom to top) of (*Z*)-**3** (5.7 mM) after addition of 32 equiv. TFA. The isomer ratio was determined by integration of the alkene H**f** signals.

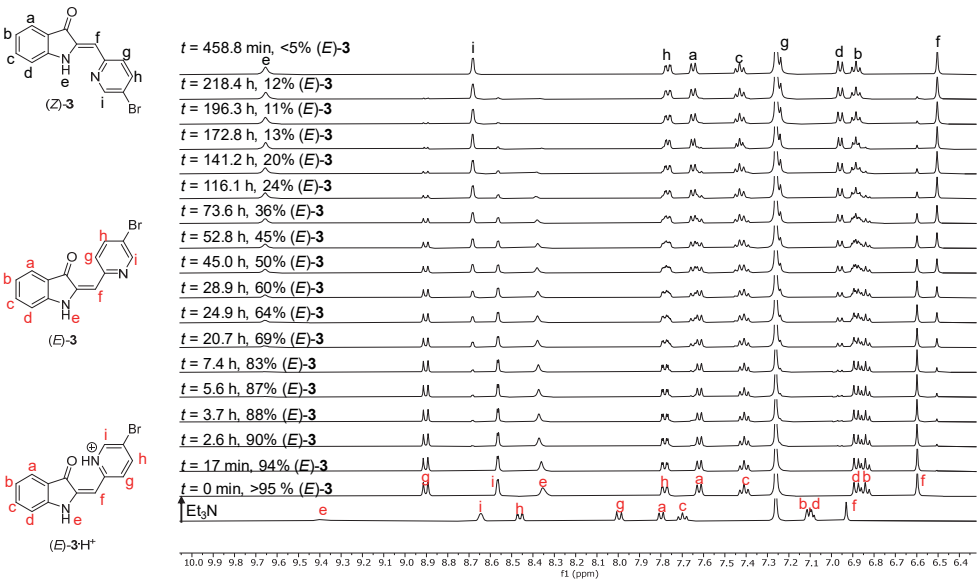

Figure E10. ^{1}H NMR spectral changes (500 and 400 MHz, $CDCl_3$) of (*E*)-**3**·**H**$^+$ (5.7 mM) equilibrated in presence of 32 equiv. TFA followed over time (from bottom to top) after addition of 48 equiv. Et_3N. The isomer ratio was determined by integration of the alkene H**f** signals.

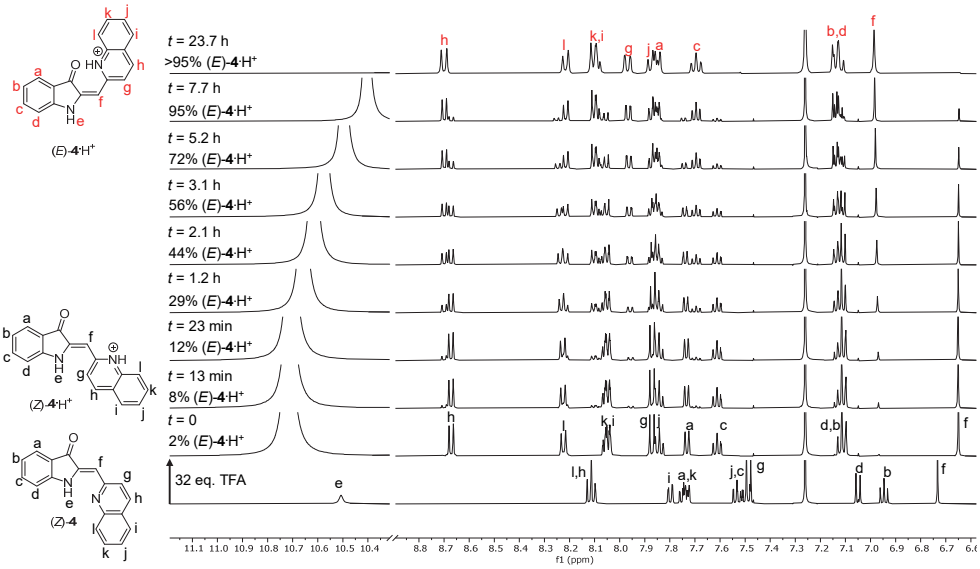

Figure E11. ^{1}H NMR spectral changes (500 MHz, $CDCl_3$) of (*Z*)-**4** (5.7 mM) followed over time (from bottom to top) after addition of 32 equiv. TFA. The isomer ratio was determined by integration of the alkene H**f** signals.

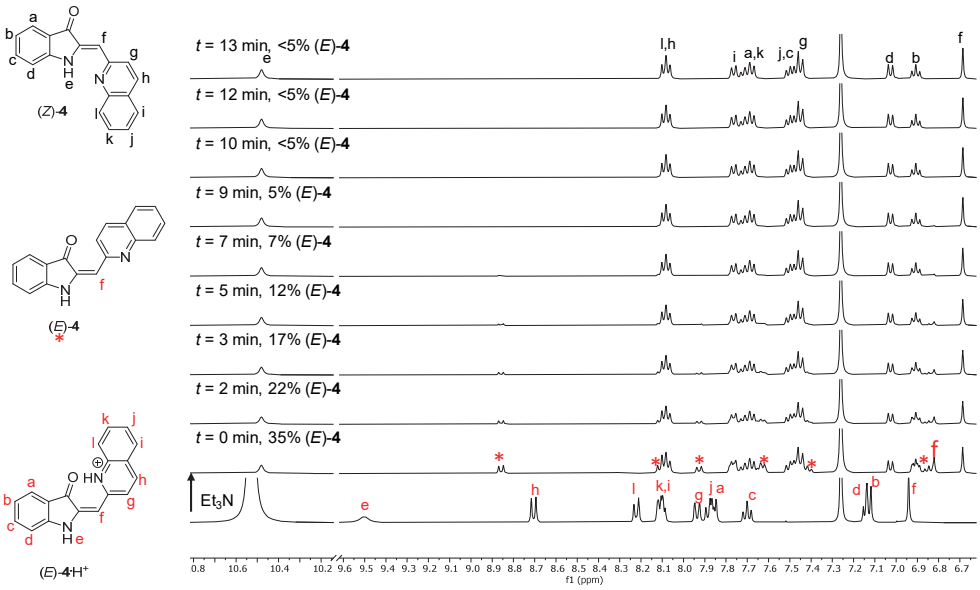

Figure E12. ^{1}H NMR spectral changes (500 and 400 MHz, $CDCl_3$) of (*E*)-**4**·**H**$^+$ (5.7 mM) equilibrated in presence of 32 equiv. TFA followed over time (from bottom to top) after addition of 48 equiv. Et_3N. The isomer ratio was determined by integration of the alkene H**f** signals. Full characterization of (*E*)-**4** was omitted due to its short thermal half-life.

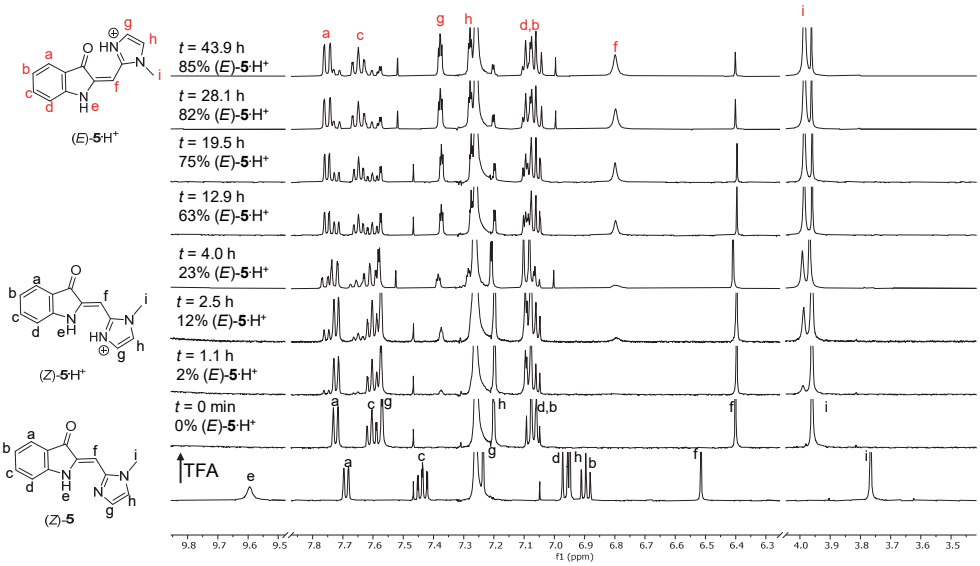

Figure E13. ^{1}H NMR spectral changes (500 and 400 MHz, $CDCl_3$) of (*Z*)-**5** (5.7 mM) followed over time (from bottom to top) in a flame-sealed NMR tube after addition of 32 equiv. TFA. The isomer ratio was determined by integration of the alkene H**f** signals.

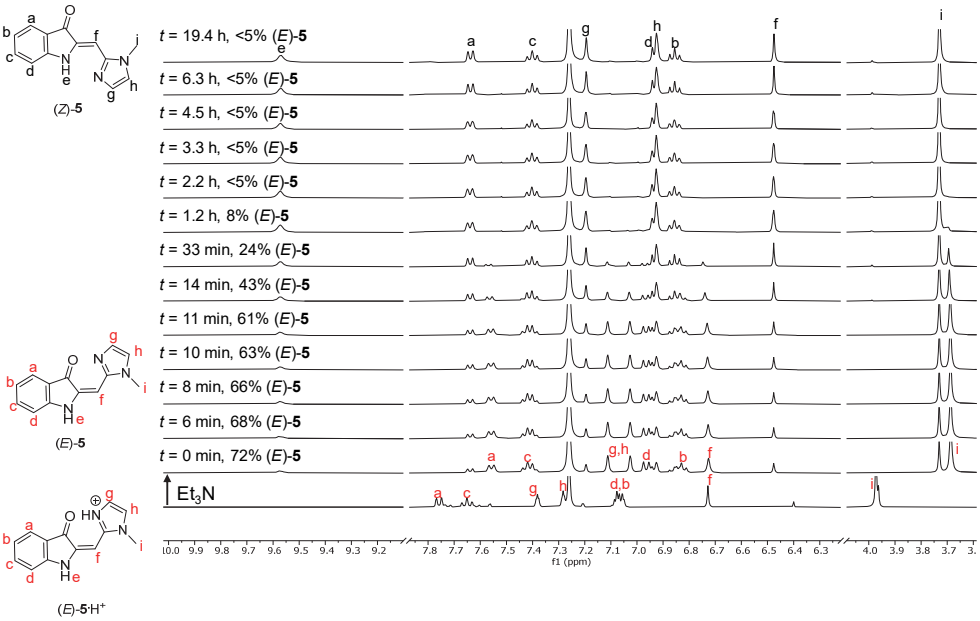

Figure E14. ^{1}H NMR spectral changes (400 MHz, $CDCl_3$) of (*E*)-**5**·**H**$^+$ (5.7 mM) equilibrated in the presence of 32 equiv. TFA followed over time (from bottom to top) after addition of 48 equiv. Et_3N. The isomer ratio was determined by integration of the alkene H**f** signals.

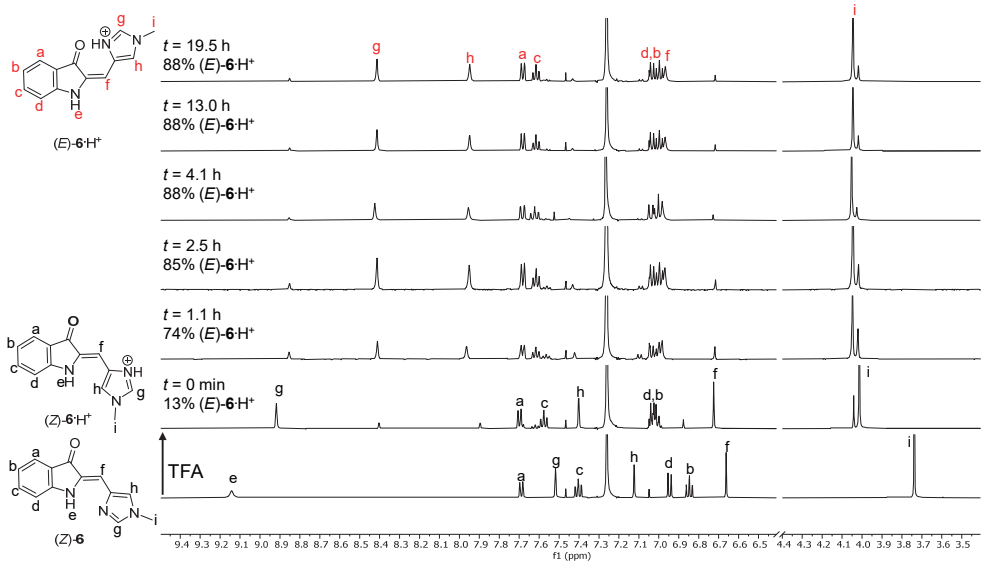

Figure E15. ^{1}H NMR spectral changes (500 MHz, $CDCl_3$) of (*Z*)-**6** (5.7 mM) followed over time (from bottom to top) in a flame-sealed NMR tube after addition of 32 equiv. TFA. The isomer ratio was determined by integration of the H**i** signals.

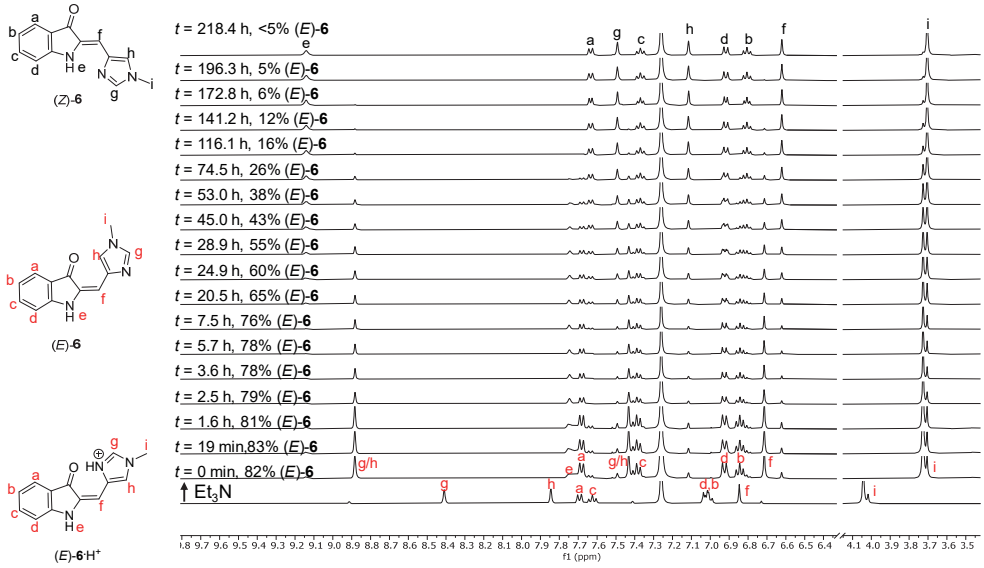

Figure E16. ^{1}H NMR spectral changes (400 and 500 MHz, $CDCl_3$) of (*E*)-**6**·**H**$^+$ (5.7 mM) equilibrated in the presence of 32 equiv. TFA followed over time (from bottom to top) after addition of 48 equiv. Et_3N. The isomer ratio was determined by integration of the alkene H**f** signals.

Fitting of ^{1}H NMR isomerization data to first-order decay kinetics

The first order decay in concentration of the protonated (*Z*)-isomer of the hemi-indigo dyes was fitted to the equation $A = A_0e^{-kt} + y0$ ($A = A_0e^{-t/t1} + y0$) using Origin software to obtain the rate constant (*k*). Data taken from Figures E1-E3 and E6-E16. Representative fit of the thermal decay on **1** have been included below.

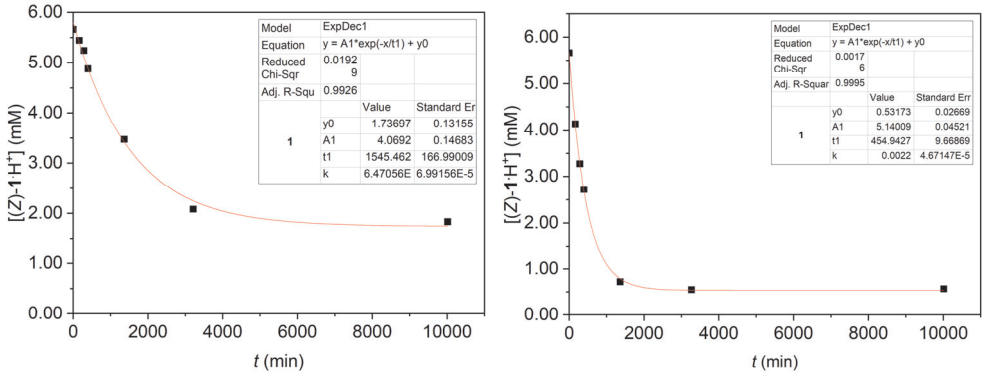

Figure E17. Change in concentration of (*Z*)-**1**·**H**$^+$ monitored over time by ^{1}H NMR (left) in the presence of 4.2 equiv. TFA. (right) in the presence of 16 equiv. TFA.

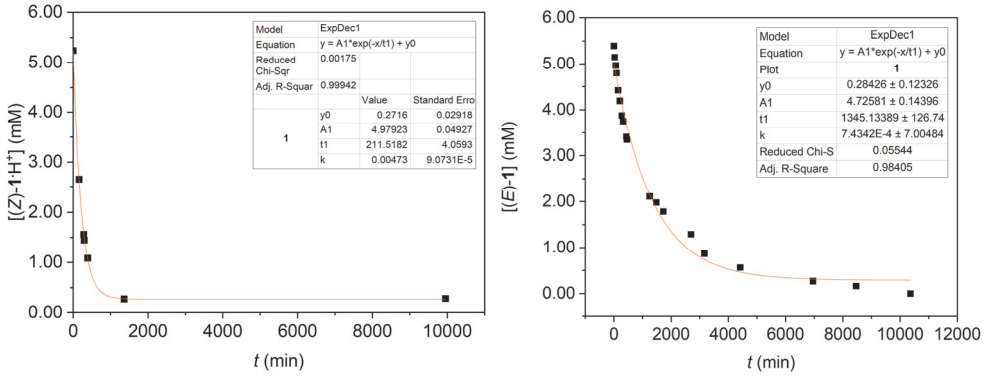

Figure E18. (left) Change in concentration of (*Z*)-**1**·**H**$^+$ monitored over time by ^{1}H NMR spectroscopy in the presence of 32 equiv. TFA. (right) Change in concentration of (*E*)-**1** monitored over time by ^{1}H NMR spectroscopy

UV-Vis Studies of Acid/Base Controlled Isomerization

Solutions of the *Z*-isomers were prepared in dried and degassed spectroscopic grade chloroform at a suitable concentration (Abs < 1.0) in a 1 mm quartz cuvette. The spectral changes were monitored over time after the addition of trifluoroacetic acid. After thermal equilibration, an excess of Et_3N was added.

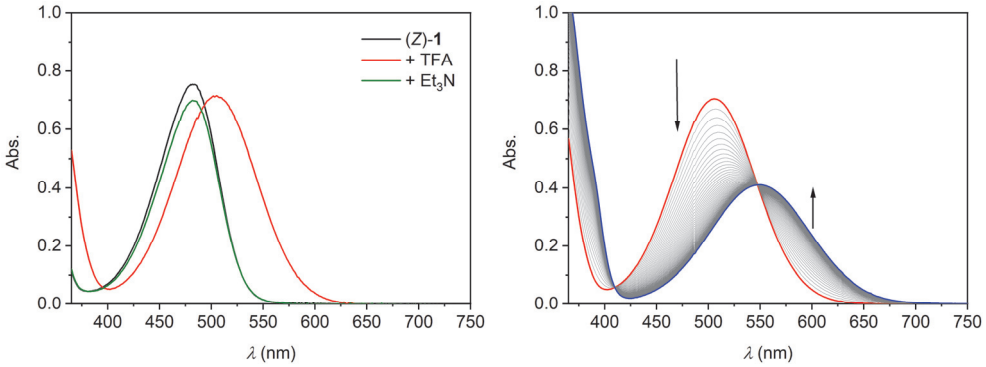

Figure E19. (left) UV-Vis spectral data showing that direct addition of TFA (4.3×10^2 equiv.) and Et_3N (1.6 equiv. with respect to TFA) to (*Z*)-**1** (0.76 mM in degassed $CHCl_3$, 1 mm cuvette) gives a similar decrease in absorbance as observed for the thermally recovered species due to dilution of the sample (initial volume: 200 µL) and potential solvatochromic effects. (right) UV-Vis spectral changes of (Z)-**1** (0.76 mM, $CHCl_3$, 1 mm cuvette) monitored over time (15 min interval) in the presence of excess TFA (4.3×10^2 equiv.).

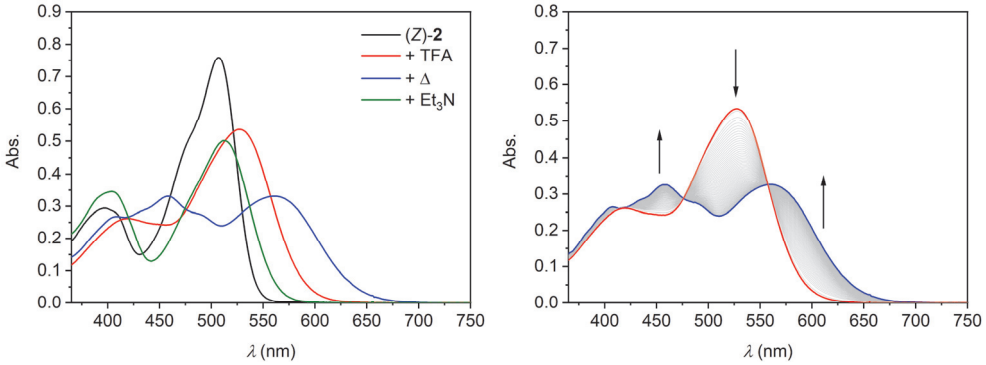

Figure E20. (left) UV-Vis spectral data of **2** (0.28 mM in degassed $CHCl_3$, 1 mm quartz cuvette) before and after addition of excess TFA (4.7×10^2 equiv.) [(*Z*)-**2**·$\mathbf{H^+}$], followed by equilibration for 16 h [Δ, enriched in (*E*)-**2**·H^+], and treatment with Et_3N (1.5 equiv. with respect to TFA) [enriched in (*E*)-**2**]. (right) UV-Vis spectral changes of (*Z*)-**2** (0.28 mM, $CHCl_3$, 1 mm cuvette) monitored over time (15 min interval) in the presence of excess TFA (4.7×10^2 equiv.).

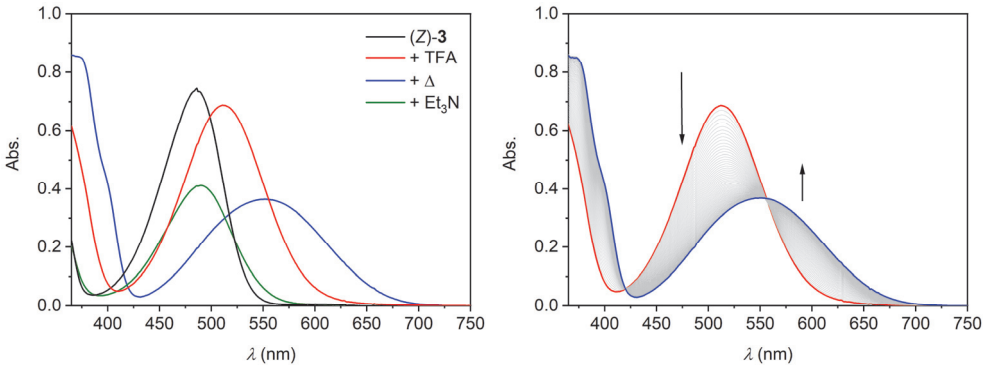

Figure E21. (left) UV-Vis spectra data of **3** (0.61 mM in degassed $CHCl_3$, 1 mm quartz cuvette) before and after addition of excess TFA (4.7×10^2 equiv.) [(*Z*)-**3**·$\mathbf{H}^+$], followed by equilibration for 16 h [Δ, enriched in (*E*)-**3**·$\mathbf{H}^+$] and treatment with Et_3N (1.0 equiv. with respect to TFA) [enriched in (*E*)-**3**].(right) UV-Vis spectral changes of (*Z*)-**3** (0.61 mM, $CHCl_3$, 1 mm cuvette) monitored over time (15 min interval) in the presence of excess TFA (4.7×10^2 equiv.).

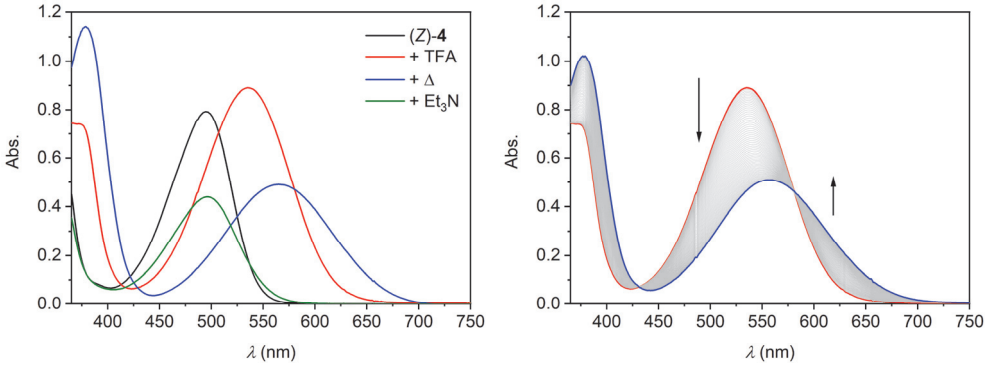

Figure E22. (left) UV-Vis spectra data of **4** (0.64 mM in degassed $CHCl_3$, 1 mm quartz cuvette) before and after addition of excess TFA (4.3×10^2 equiv.) [(*Z*)-**4**·$\mathbf{H}^+$], followed by equilibration for 16 h [Δ, enriched in (*E*)-**4**·$\mathbf{H}^+$], and treatment with Et_3N (4.0 equiv. with respect to TFA) [enriched in (*E*)-**4**]. (right) UV-Vis spectral changes of (*Z*)-**4** (0.64 mM, $CHCl_3$, 1 mm cuvette) monitored over time (15 min interval) in the presence of excess TFA (4.3×10^2 equiv.).

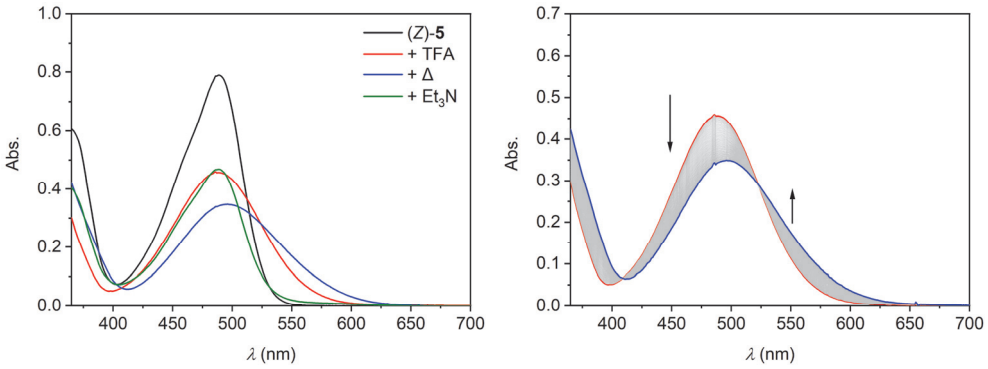

Figure E23. (left) UV-Vis spectra data of **5** (0.71 mM in degassed $CHCl_3$, 1 mm quartz cuvette) before and after addition of excess TFA (3.7×10^2 equiv.) [(*Z*)-**5**·**H**$^+$], followed by equilibration for 16 h [Δ, enriched in (*E*)-**5**·**H**$^+$], and treatment with Et_3N (4.2 equiv. with respect to TFA) [enriched in (*E*)-**5**]. (right) UV-Vis spectra data of **5** (0.71 mM in degassed $CHCl_3$, 1 mm quartz cuvette) before and after addition of excess TFA (3.7×10^2 equiv.) [(*Z*)-**5**·**H**$^+$], followed by equilibration for 16 h [Δ, enriched in (*E*)-**5**·**H**$^+$], and treatment with Et_3N (4.2 equiv. with respect to TFA) [enriched in (*E*)-**5**].

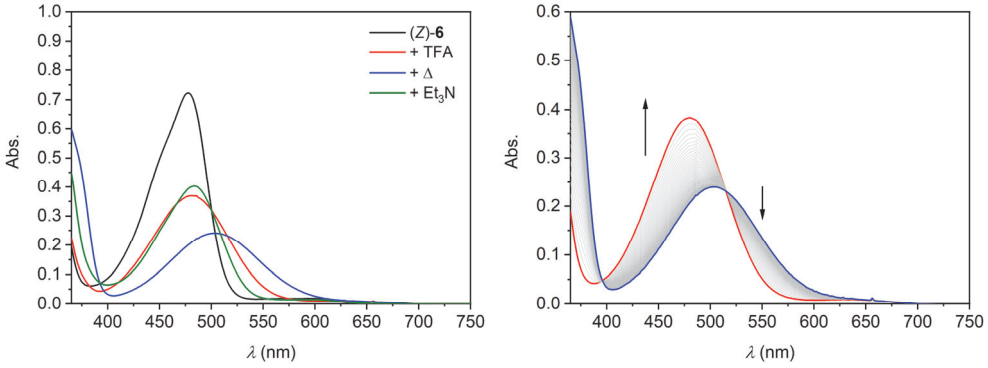

Figure E24. (left) UV-Vis spectra data of **6** (0.89 mM in degassed $CHCl_3$, 1 mm quartz cuvette) before and after addition of excess TFA (3.7×10^2 equiv.) [(*Z*)-**6**·**H**$^+$], followed by equilibration for 16 h [Δ, enriched in (*E*)-**6**·**H**$^+$], and treatment with Et_3N (4.2 equiv. with respect to TFA) [enriched in (*E*)-**6**]. (right) UV-Vis spectral changes of (*Z*)-**6** (0.89 mM, $CHCl_3$, 1 mm cuvette) monitored over time (15 min interval) in presence of excess TFA (3.7×10^2 equiv.).

UV-Vis Photoisomerization Studies

All UV-Vis spectra were recorded at 273 K (or lower if specified) to minimize the effect of thermal isomerization. Samples of (*E*)-isomers were prepared from the (*Z*)-isomer by irradiation in the presence of TFA or, in the case of compound **6**, by thermal equilibration in the presence of excess TFA (left overnight) at the same concentration as at which the ^{1}H NMR experiments were performed.

Note: In comparison to the photochemical isomerization, it appears that lower conversion was achieved upon thermal isomerization in the UV-Vis experiments than in the ^{1}H NMR experiments For example, for compound **1**, the spectrum for the photochemically generated species [(*E*)-**1**·H$^+$] is further red-shifted than was observed after the thermally activated process ($\lambda_{max,thermal}$ = 549 nm vs $\lambda_{max,photochemical}$ = 566 nm vs $\lambda_{max,TD\text{-}DFT}$ = 554 nm). The thermal isomerization process may be affected by incomplete protonation, the different nature of the pyridinium-carboxylate ion pair and/or the increased dielectric constant of the medium in the presence of the larger excess of TFA necessary for protonation at the lower concentration used in the UV-Vis experiments.

Photoisomerization of 1

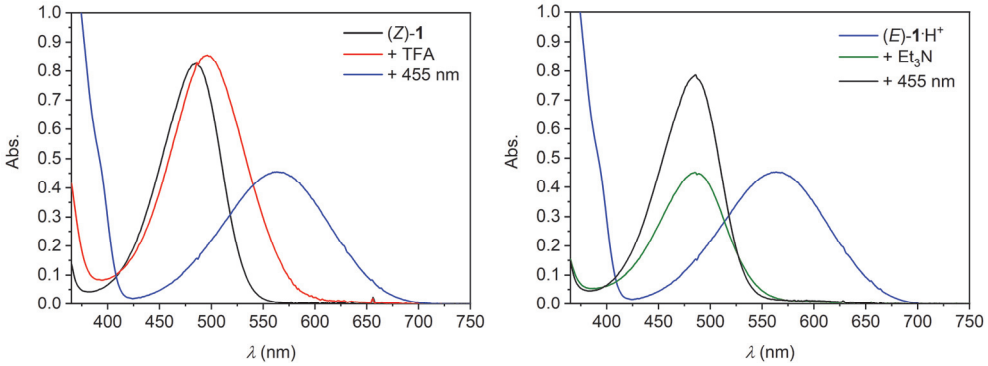

Figure E25. (left) UV-Vis spectra starting with (*Z*)-**1** (0.076 mM in degassed $CHCl_3$, 1 cm quartz cuvette), where irradiation with 365 nm, 385 nm, 455 nm, 465 nm, 525 nm, for 2-10 min did not cause any spectral changes, yet after addition of TFA (4.7×10^2 equiv.) and irradiation with 455 nm photoisomerization occurred. (right) UV-Vis spectrum of (*E*)-**1**·**H**$^+$ (0.076 mM in degassed $CHCl_3$, formed by 455 nm irradiation at a concentration of 0.076 mM in presence of 4.7×10^2 eq TFA), where irradiation with 365 nm, 385 nm, 455 nm, 465 nm, 525 nm, 591 nm, 630 nm, and 660 nm for 2-10 min did not cause any further spectral changes. After addition of Et_3N (7.0×10^2 equiv.) and irradiation at 455 nm photoisomerization to (*Z*)-**1** took place.

Photoisomerization of 2

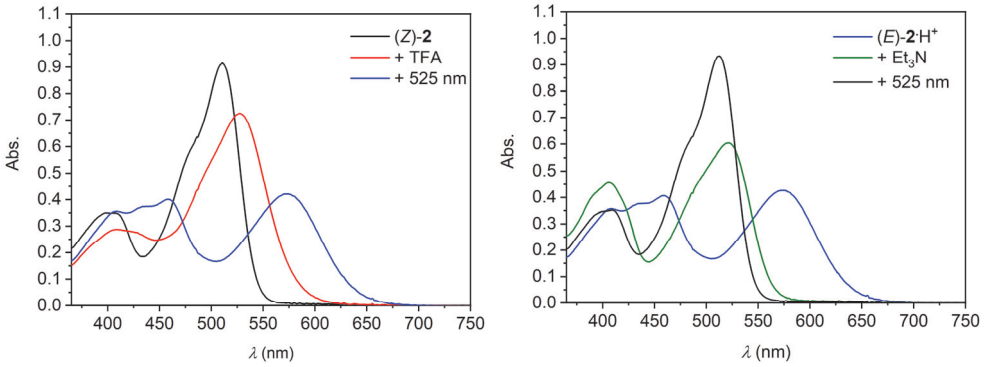

Figure E26. (left) UV-Vis spectra starting with (*Z*)-**2** (0.028 mM in degassed $CHCl_3$, 1 cm quartz cuvette), where irradiation with 405 nm, 455 nm, 465 nm, 525 nm for 6 min did not cause any spectral changes, yet after addition of TFA (4.7×10^2 equiv.) and irradiation with 525 nm photoisomerization occurred. (right) UV-Vis spectrum of (*E*)-**2**·$\mathbf{H^+}$ at 263 K (0.028 mM in degassed $CHCl_3$, formed by irradiation using 525 nm light at a concentration of 0.028 mM in presence of 4.7×10^2 equiv. TFA), where irradiation with 405 nm, 455 nm, 525 nm, 591 nm, 630 nm or 660 nm for 6 min did not cause any further spectral changes. After addition of Et_3N (7.0×10^2 equiv.) and irradiation at 525 nm photoisomerization to (*Z*)-**2** took place.

Photoisomerization of 3

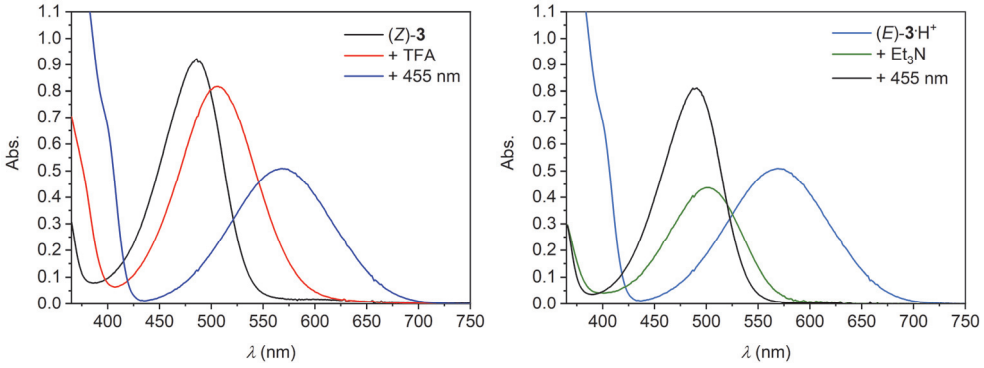

Figure E27. (left) UV-Vis spectra starting with (*Z*)-**3** (0.073 mM in degassed $CHCl_3$, 1 cm quartz cuvette), where irradiation with 405 nm, 455 nm, 525 nm, or 591 nm for 2-10 min did not cause any spectral changes, yet after addition of TFA (2.4×10^3 equiv.) and irradiation with 455 nm photoisomerization occurred. (right) UV-Vis spectrum of (*E*)-**3**·$\mathbf{H^+}$ (0.073 mM in degassed $CHCl_3$, formed by irradiation using 455 nm light at a concentration of 0.073 mM in presence of 2.4×10^3 equiv. TFA), where irradiation with 405 nm, 455 nm, 525 nm, or 591 nm for 2-10 min did not cause any further spectral changes. After addition of Et_3N (3.7×10^3 equiv.) and irradiation with 525 nm photoisomerization to (*Z*)-**3** took place.

Photoisomerization of 4

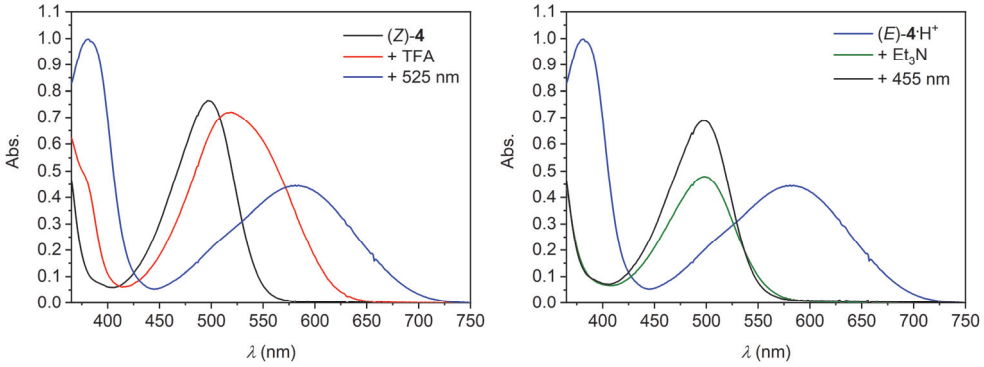

Figure E28. (Left) UV-Vis spectra starting with (*Z*)-**4** (0.051 mM in degassed $CHCl_3$, 1 cm quartz cuvette), where irradiation with 405 nm, 455 nm, 465 nm, 525 nm for 2-10 min did not cause any spectral changes, yet after addition of TFA (4.7×10^2 equiv.) and irradiation with 525 nm photoisomerization occurred. (right) UV-Vis spectrum of (*E*)-**4**·$\mathbf{H}^+$ at 263 K (0.051 mM in degassed $CHCl_3$, formed by irradiation using 525 nm light at a concentration of 0.051 mM in presence of 4.7×10^2 equiv. TFA), where irradiation with 455 nm, 525 nm and 591 nm for 2-10 min did not cause in any further spectral changes. After addition of Et_3N (7.0×10^2 equiv.) and irradiation with 455 nm photoisomerization to (*Z*)-**4** took place.

Photoisomerization of 5

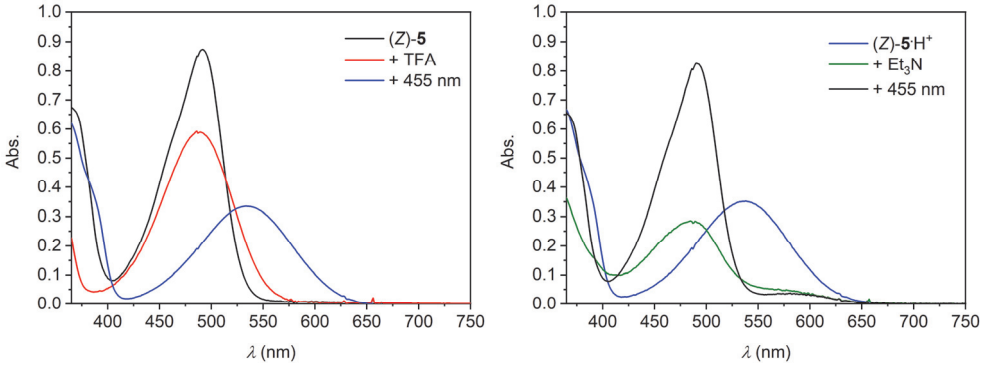

Figure E29. (left) UV-Vis spectra starting with (*Z*)-**5** (0.071 mM in degassed $CHCl_3$, 1 cm quartz cuvette), where irradiation with 455 nm, 465 nm, 525 nm for 2-10 min did not cause any spectral changes, yet after addition of TFA (4.7×10^2 equiv.) and irradiation with 455 nm photoisomerization occurred. (right) UV-Vis spectrum of (*E*)-**5**·$\mathbf{H}^+$ 263 K (0.071 mM in degassed $CHCl_3$, formed by irradiation using 455 nm light at a concentration of 0.071 mM in presence of 4.7×10^2 equiv. TFA), where irradiation with 455 nm, 465 nm, 525 nm and 591 nm for 2-10 min did not cause in any spectral changes. After addition of Et_3N (2.0×10^3 equiv.) and irradiation with 455 nm photoisomerization to (*Z*)-**5** took place (alternatively 465 nm or 525 nm light could be used).

Photoisomerization of 6

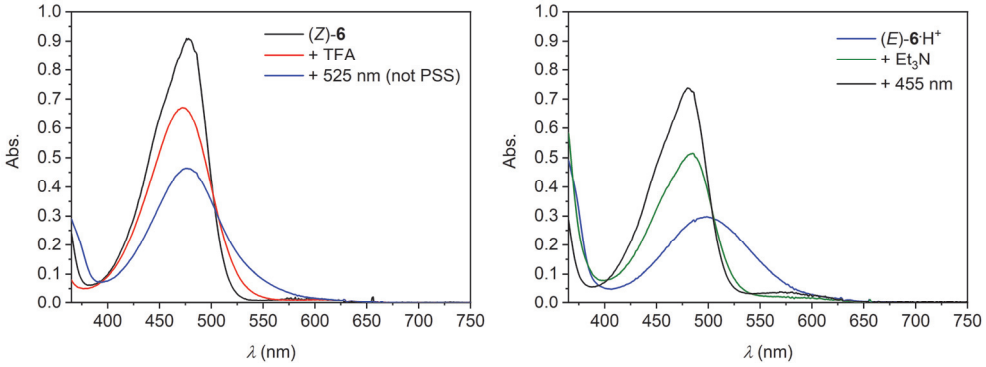

Figure E30. (left) UV-Vis spectra starting with (*Z*)-**6** (0.088 mM in degassed $CHCl_3$, 1 cm quartz cuvette), where irradiation with 525 nm for 2-10 min did not cause any spectral changes, but irradiation with 405 and 455 nm for 2-12 min resulted in minor decomposition (<5%, see Figure E31). After addition of TFA (4.7×10^2 equiv.) and irradiation with 455 nm photoisomerization and decomposition occurred (see Figure E31), irradiation with 525 nm afforded clean photoisomerization, however, the PSS was not yet reached after 80 minutes due to slow photoisomerization. (right) UV-Vis spectrum of (*E*)-**6**·$\mathbf{H^+}$ (0.088 mM in degassed $CHCl_3$, which was formed by thermal equilibration at 4.8 mM concentration in presence of 4.7×10^2 eq TFA), where irradiation with 405 nm and 455 nm for 2 min did not cause any significant spectral changes. After addition of Et_3N (7.0×10^2 equiv.) and irradiation with 455 nm photoisomerization to (*Z*)-**6** took place.

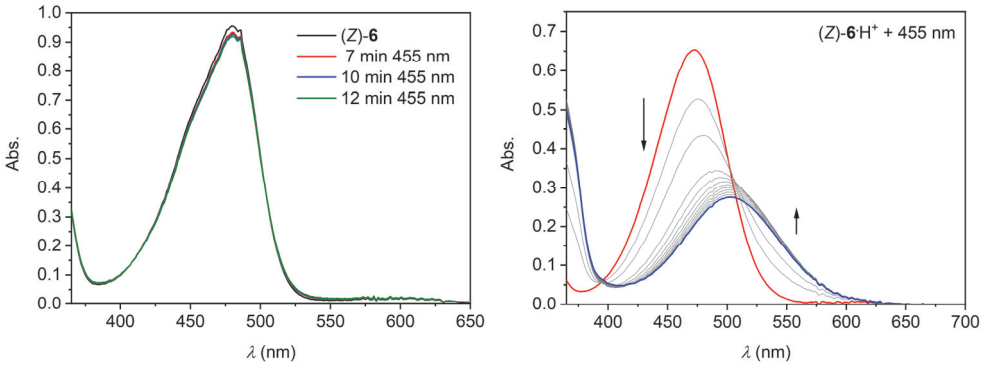

Figure E31. (left) UV-VIS spectra of (*Z*)-**6** under continuous irradiation at 455 nm. (right) UV-Vis spectra of (*Z*)-**6**·$\mathbf{H^+}$ under continuous irradiation with 455 nm showing concomitant photoisomerization and photodegradation. Spectra were taken every 5 min under the experimental conditions described in Figure E30 (left).

Table E7. Overview of UV-Vis absorption maxima of **1-6** alongside wavelengths that could be used for photoisomerization.

	Z λ_{max} =	*Z*·H$^+$ λ_{max} =	*Z*·H$^+$→*E*·H$^+$ λ_{irrad} =	*E*·H$^+$ λ_{max} =	*E*[b] λ_{max} =	*E*→*Z* λ_{irrad} =
1	485 nm	496 nm	455nm	566 nm	486 nm	455 nm
2	511 nm	528 nm	525 nm	573 nm	521 nm	525 nm
3	486 nm	507 nm	455 nm	567 nm	500 nm	455 nm
4	496 nm	519 nm	455 nm	581 nm	498 nm	455 nm
5	490 nm	486 nm	455 nm	538 nm	489 nm	455 nm
6	476 nm	472 nm	525 nm	499 nm[a]	485 nm[a]	455 nm

[a](*E*)-**6**·**H**$^+$ thermally generated due to exceedingly slow photoisomerization. [b]Note that partial thermal isomerization upon exothermic basification to the *Z*-isomer cannot be excluded

^{1}H NMR photoisomerization studies

A solution of **1** (5.6 mM) was prepared in degassed, dried $CDCl_3$. The solution was transferred to a J-Young NMR tube, and TFA was added (3.0 equiv.). The solution was subsequently irradiated after tightly closing the J-Young valve in order to avoid TFA evaporation.

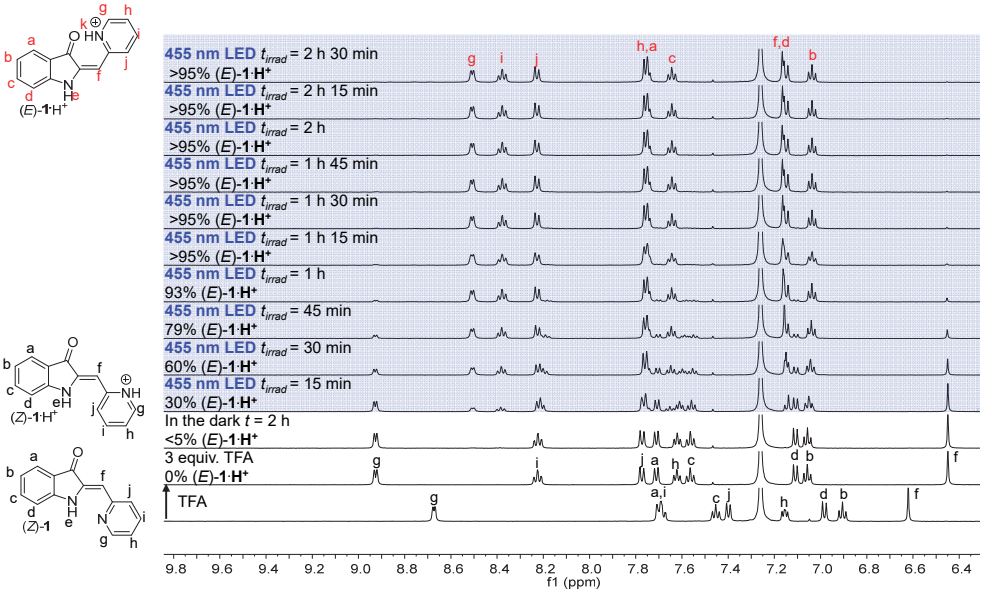

Figure E32. ^{1}H NMR (500 MHz) spectra showing photochemical generation of (*E*)-**1**·**H**$^+$ from (*Z*)-**1**·**H**$^+$ (5.6 mM, $CDCl_3$) in presence of TFA (3.0 eq) by irradiation with 455 nm. Less TFA is used here than in the thermal isomerization experiments (32 equiv.) to lower thermal conversion to (*E*)-**1**·**H**$^+$ and reduce the rate of this process.

Quantum Yield Determination

The photon flux of the used Thorlabs model M455F3 high-power LED (λ_{max} = 455 nm) was determined at maximum power by measuring the production of ferrous ions from potassium ferrioxalate.[48] Solutions of potassium ferrioxalate (150 mM in 0.05 M H_2SO_4) were irradiated for a defined period of time with the LED in a dark environment, after which an aliquot (0.5 mL) of the irradiated solution was added to 2.0 mL of a buffered solution of 1,10-phenanthroline (0.1 wt% phenanthroline in 0.5 M H_2SO_4 buffered with 1.65 M sodium acetate). The mixture was equilibrated in the dark for 30 minutes, after which the characteristic absorbance of the Fe^{2+} complex ($Fe[phen]_3^{2+}$) at 510 nm was measured (ε_{510}= 1.11× 10^4 M^{-1} cm^{-1}). The number of moles of Fe^{2+} ions produced was determined at four different irradiation times, and the slope of a plot of the molar amount of Fe^{2+} ions versus time corresponds to the rate of Fe^{2+} ion formation, which was found to be 4.46 × 10^{-8} mol s^{-1}.

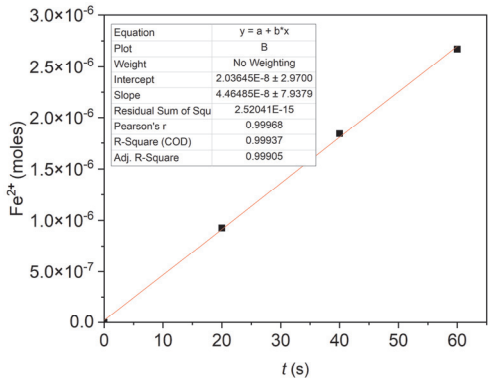

Figure E33. Moles of Fe^{2+} ions produced after irradiation of a 0.15 M ferrioxalate solution at 455 nm in a 1 cm quartz cuvette at 293 K, and linear data fitting to determine the slope.

The rate of Fe^{2+} ion formation was used to calculate the photon flux with equation E1:[48,49]

$$\text{Photon flux (mol s}^{-1}) = \frac{dFe^{2+}}{dt} \times \frac{1}{\phi} \qquad \text{(Eq. E1)}$$

Where the closest reported quantum yield of ferrioxalate (ϕ = 1.09 at 457.9 nm)[50] was taken, and the fraction of light absorbed by the ferrioxalate solution is given by $F = 1 - 10^{-\text{Abs(455 nm)}}$.[49] Using these values (F=0.957 in this case), the photon flux was calculated as 4.28 × 10^{-8} mol s^{-1}. Photoisomerization of compounds **1-5** was followed in the same irradiation set-up as the ferrioxalate solution, and the rates of new isomer formation and the previously determined photon flux were used to calculate the quantum yields by the following equation:

$$\phi = \frac{\text{Rate of isomer formation (mol s}^{-1})}{\text{photon flux (mol s}^{-1})} \qquad \text{(Eq. E2)}$$

The quantum yield of (*Z*)·H⁺-to-(*E*)·H⁺ photoisomerization was determined by first preparing solutions of the respective (*Z*)-isomer in degassed $CHCl_3$ and followed by the addition of 470 equiv. of TFA at 0° C. The concentrations were such that all incoming light was absorbed (Abs ≥ 2.0 at 455 nm). Upon irradiation with 455 nm light, the change in absorbance was followed at a wavelength at which the absorbance is linear with concentration (Abs < 1.0). This change in absorbance was then used to calculate the concentration increase of (*E*)-isomer, by using the known molar absorptivity (ε) at the selected wavelength using equation E3.

$$\Delta[(E)\cdot \mathrm{H}^+] = \frac{\Delta Abs(\lambda)}{\varepsilon\{[(E)\cdot \mathrm{H}^+),\lambda\} - \varepsilon\{(Z)\cdot \mathrm{H}^+),\lambda\}} \qquad \text{(Eq. E3)}$$

To determine the quantum yield of *E*-to-*Z* photoisomerization, first solutions of (*E*)·H⁺ were prepared by thermally equilibrating solutions of the respective *Z*-isomer at 5.7 mM in the presence of 32 equiv. of TFA, similar to that performed for the ^{1}H NMR thermal isomerization experiments. The samples were subsequently diluted in $CHCl_3$ that was acidified with TFA, to reach a sample with a total of 470 equiv. of TFA. The sample was then cooled to 0° C or –10 °C, and Et_3N was added (1.5 equiv. with respect to TFA). Again, the concentrations were such that all incoming light was absorbed (Abs ≥ 2.0 at 455 nm). The *in situ* formed *E*-isomer was then irradiated with 455 nm light, and also in this case, the change in absorbance was followed at a wavelength at which the absorbance was linear with concentration (Abs < 1.0). This change in absorbance was used to calculate the increase in the concentration of *Z*-isomer, by using the known molar absorptivity at the selected wavelength (Equation E4).

$$\Delta[(Z)] = \frac{\Delta Abs(\lambda)}{\varepsilon\{(Z),\lambda\} - \varepsilon\{(E),\lambda\}} \qquad \text{(Eq. E4)}$$

Representative kinetic measurements for the formation of (*E*)-**1**·H⁺ and (Z)-**1**·H⁺ have been included below.

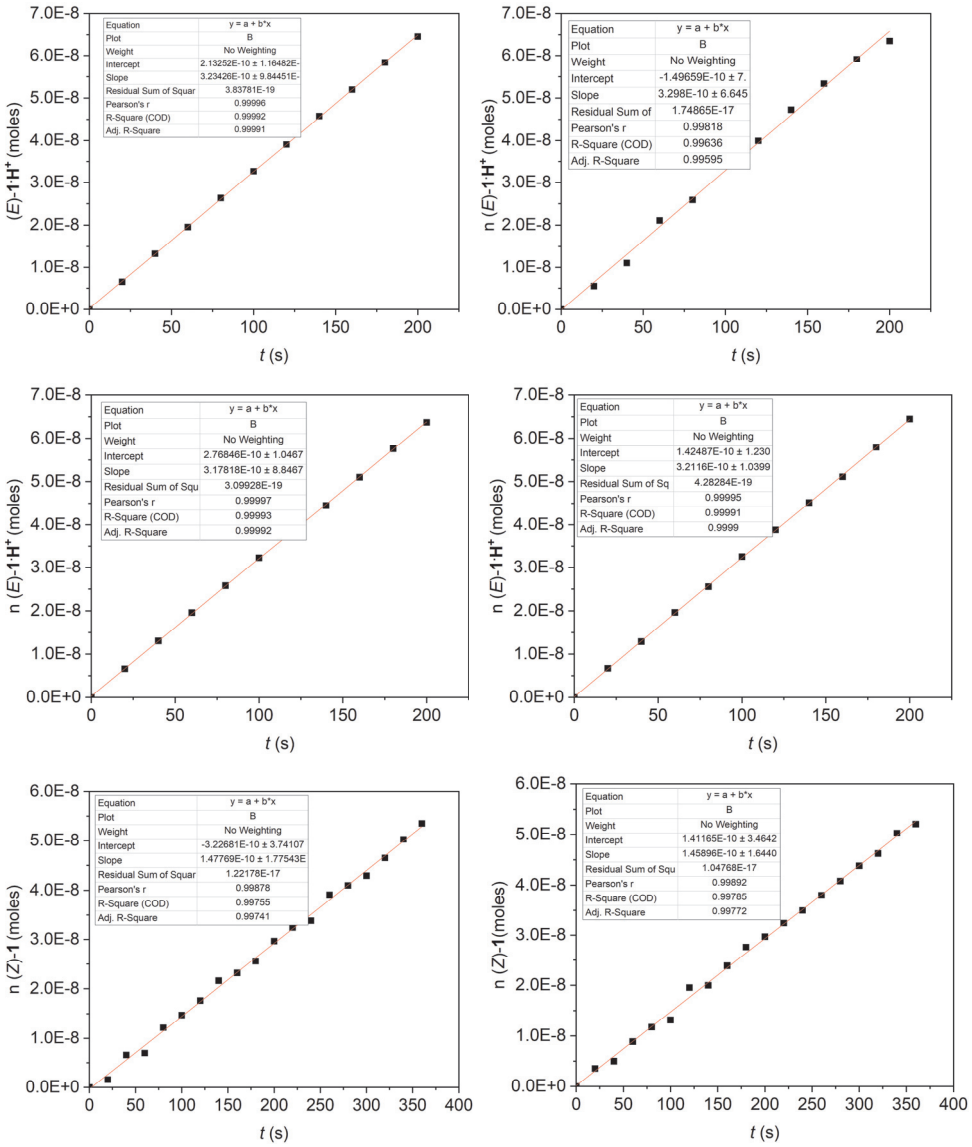

Figure E34. (top) Duplicate measurements of formation of (*E*)-**1**·H$^+$ upon irradiation of an aerated solution of (*Z*)-**1** (0.55 mM, 2 mL $CHCl_3$, 1 cm quartz cuvette, 273 K) with 455 nm light in the presence of 470 equiv. TFA. Rates of formation: 3.23×10^{-10} mol s^{-1} and 3.30×10^{-10} mol s^{-1} (middle) Duplicate measurements of formation of (*E*)-**1**·H$^+$ upon irradiation of a degassed solution of (*Z*)-**1** (0.55 mM, 2 mL $CHCl_3$, 1 cm quartz cuvette, 273 K) with 455 nm light in the presence of 470 equiv. TFA. Rates of formation: 3.18×10^{-10} mol s^{-1} and 3.21×10^{-10} mol s^{-1}. (bottom) Duplicate measurements of formation of (*Z*)-**1** upon irradiation of a degassed solution of (*E*)-**1** (0.55 mM, 2 mL degassed $CHCl_3$, 1 cm quartz cuvette, 273 K) with 455 nm light in the presence of 470 equiv. TFA and 700 equiv. of Et_3N. Rate of formation: 1.48×10^{-10} mol s^{-1} and 1.46×10^{-10} mol s^{-1}

Computational Details

All calculations were performed using Gaussian 09,[51] and data was visualized using Avogadro 1.2.0[52] and Gaussview 6.[53] Geometry optimizations were performed at the B3LYP 6-311++G(d,p) level of theory using an IEFPCM solvation model ($CHCl_3$). All computed stationary points were subjected to frequency analysis and confirmed as local minima through analytical computation of force constants (no imaginary frequencies found for all minima). UV-Vis spectra were calculated by TD-DFT on the B3LYP 6-311++G(d,p) level of theory with non-equilibrium IEFPCM ($CHCl_3$), solving for the first 30 singlet excited states for the most stable conformers of the configurational isomers of **1**. This level of theory has been previously used to describe the related hemi-thioindigo[54] scaffold, and a similar approach proved accurate for hemi-indigo (PCM-TD-B3LYP/6-311+G(2d,p)//PCM-B3LYP/6-311(d,p)).[55]

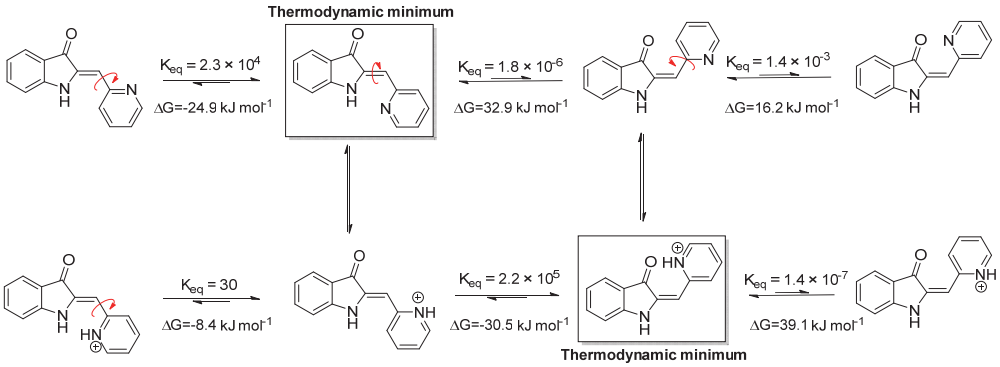

Scheme E1. Overview of relative energies of **1**. Calculated at B3LYP 6-311++G(d,p) level of theory with an IEFPCM $CHCl_3$ solvent model.

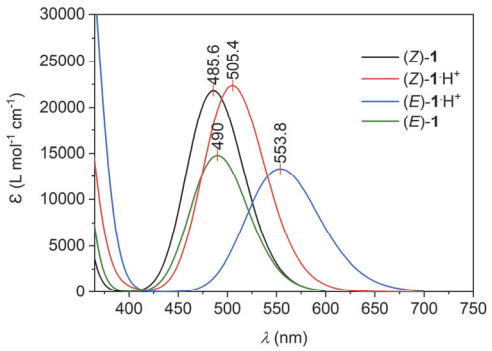

Figure E35. Predicted UV-Vis spectra of optimized (*Z*)-**1** A, (*E*)-**1** B, (*Z*)-**1**·**H**$^+$ B, and (*E*)-**1**·**H**$^+$ A (n=30 states, TD-DFT, B3LYP 6-311++G(d,p), IEF-PCM $CHCl_3$) with line-broadening set at 0.177 eV with peaks annotated.

2.9 References

[1] H. Luecke, B. Schobert, H.-T. Richter, J.-P. Cartailler, J. K. Lanyi, *Science* **1999**, *286*, 255–260.

[2] K. Edman, P. Nollert, A. Royant, H. Belrhali, E. Pebay-Peyroula, J. Hajdu, R. Neutze, E. M. Landau, *Nature* **1999**, *401*, 822–826.

[3] S. Subramaniam, R. Henderson, *Nature* **2000**, *406*, 653–657.

[4] G. Steinberg-Yfrach, P. A. Liddell, S.-C. Hung, A. L. Moore, D. Gust, T. A. Moore, *Nature* **1997**, *385*, 239–241.

[5] S. Bhosale, A. L. Sisson, P. Talukdar, A. Fürstenberg, N. Banerji, E. Vauthey, G. Bollot, J. Mareda, C. Röger, F. Würthner, N. Sakai, S. Matile, *Science* **2006**, *313*, 84–86.

[6] X. Xie, G. A. Crespo, G. Mistlberger, E. Bakker, *Nat. Chem.* **2014**, *6*, 202–207.

[7] V. Balzani, A. Credi, F. M. Raymo, J. F. Stoddart, *Angew. Chem. Int. Ed.* **2000**, *39*, 3348–3391.

[8] W. R. Browne, B. L. Feringa, *Nat. Nanotechnol.* **2006**, *1*, 25–35.

[9] S. Erbas-Cakmak, D. A. Leigh, C. T. McTernan, A. L. Nussbaumer, *Chem. Rev.* **2015**, *115*, 10081–10206.

[10] M. A. Watson, S. L. Cockroft, *Chem. Soc. Rev.* **2016**, *45*, 6118-6129.

[11] I. Aprahamian, *ACS Cent. Sci.* **2020**, *6*, 347–358.

[12] H. Li, C. Cheng, P. R. McGonigal, A. C. Fahrenbach, M. Frasconi, W.-G. Liu, Z. Zhu, Y. Zhao, C. Ke, J. Lei, R. M. Young, S. M. Dyar, D. T. Co, Y.-W. Yang, Y. Y. Botros, W. A. Goddard III, M. R. Wasielewski, R. D. Astumian, J. F. Stoddart, *J. Am. Chem. Soc.* **2013,** *135*, 18609–18620.

[13] G. Ragazzon, M. Baroncini, S. Silvi, M. Venturi, A. Credi, *Nat. Nanotechnol.* **2015**, *10*, 70–75.

[14] M. Canton, J. Groppi, L. Casimiro, S. Corra, M. Baroncini, S. Silvi, A. Credi, *J. Am. Chem. Soc.* **2021**, *143*, 10890–10894.

[15] C. Cheng, P. R. McGonigal, S. T. Schneebeli, H. Li, N. A. Vermeulen, C. Ke, J. F. Stoddart, *Nat. Nanotechnol.* **2015**, *10*, 547–553.

[16] S. Amano, S. D. P. Fielden, D. A. Leigh, *Nature* **2021**, *594*, 529-534.

[17] Y. Qiu, Y. Feng, Q.-H. Guo, R. D. Astumian, J. F. Stoddart, *Chem* **2020**, *6*, 1952–1977.

[18] Y. Feng, M. Ovalle, J. S. W. Seale, C. K. Lee, J. D. Kim, R. D. Astumian, J. F. Stoddart, *J. Am. Chem. Soc.* **2021**, *143*, 5569–5591.

[19] K. Nakashima, A. Georgiev, D. Yordanov, Y. Matsushima, S.-I. Hirashima, T. Miura, L. Antonov, *J. Org. Chem.* **2022**, *87*, 6794–6806.

[20] C. Pezzato, C. Cheng, J. F. Stoddart, R. D. Astumian, *Chem. Soc. Rev.* **2017**, *46*, 5491–5507.

[21] S. Goldup, I. Aprahamian, *J. Am. Chem. Soc.* **2023**, *145*, 14169–14183.

[22] V. Serreli, C.-F. Lee, E. R. Kay, D. A. Leigh, *Nature* **2007**, *445*, 523–527.

[23] C. Petermayer, S. Thumser, F. Kink, P. Mayer, H. Dube, *J. Am. Chem. Soc.* **2017**, *139*, 15060–15067.
[24] M. Ikegami, T. Arai, *Bull. Chem. Soc. Jpn.* **2003**, *76*, 1783–1792.
[25] M. Ikegami, T. Suzuki, Y. Kaneko, T. Arai, *Mol. Cryst. Liq. Cryst. Sci. Technol., Sect. A*. **2000**, *345*, 113–118.
[26] V. Josef, F. Hampel, H. Dube, *Angew. Chem. Int. Ed.* **2022**, *61*, e202210855.
[27] M. Krell-Jørgensen, H. Zulfikri, M. G. Bonnevie, F. S. Bro, A. O. Dohn, L. Laraia, *Chem. Commun.* **2023**, *59*, 563–566.
[28] J. E. Zweig, T. R. Newhouse, *J. Am. Chem. Soc.* **2017**, *139*, 10956–10959.
[29] M. N. Chaur, D. Collado, J.-M. Lehn, *Chem. Eur. J.* **2011**, *17*, 248–258.
[30] S. M. Landge, I. Aprahamian, *J. Am. Chem. Soc.* **2009**, *131*, 18269–18271.
[31] E. C. Nicholls-Allison, G. Nawn, B. O. Patrick, R. G. Hicks, *Chem. Commun.* **2015**, *51*, 12482–12485.
[32] U. Burger, A. O. Bringhen, *Helv. Chim. Acta* **1989**, *72*, 93–100.
[33] E. R. Berg, D. D. Green, D. C. Moliva A., B. T. Bjerke, M. W. Gealy, D. J. Ulness, *J. Phys. Chem. A* **2008**, *112*, 833–838.
[34] C. Dolain, V. Maurizot, I. Huc, *Angew. Chem. Int. Ed.* **2003**, *42*, 2738–2740.
[35] A. D. Allen, M. Rosenbaum, N. O. L. Seto, T. T. Tidwell, *J. Org. Chem.* **1982**, *47*, 4234–4239.
[36] T. Hao, Y. Yang, W. Liang, C. Fan, X. Wang, W. Wu, X. Chen, H. Fu, H. Chen, C. Yang, *Chem. Sci.* **2021**, *12*, 2614–2622.
[37] D. Villarón, N. Duindam, S. J. Wezenberg, *Chem. Eur. J.* **2021**, *27*, 17346–17350.
[38] M. Sacherer, F. Hampel, H. Dube, *Nat. Commun.* **2023**, *14*, 4382.
[39] S. Wiedbrauk, H. Dube, *Tetrahedron Lett.* **2015**, *56*, 4266–4274.
[40] J. Pina, D. Sarmento, M. Accoto, P. L. Gentili, L. Vaccaro, A. Galvão, J. S. Seixas de Melo, *J. Phys. Chem. B* **2017**, *121*, 2308–2318.
[41] K. Yumoto, M. Irie, K. Matsuda, *Org. Lett.* **2008**, *10*, 2051–2054.
[42] I. C.-Y. Hou, F. Berger, A. Narita, K. Müllen, S. Hecht, *Angew. Chem. Int. Ed.* **2020**, *59*, 18532–18536.
[43] M. Medved', M. W. H. Hoorens, M. Di Donato, A. D. Laurent, J. Fan, M. Taddei, M. Hilbers, B. L. Feringa, W. J. Buma, W. Szymanski, *Chem. Sci.* **2021**, *12*, 4588–4598.
[44] S. J. Wezenberg, *Chem. Commun.* **2022**, *58*, 11045–11058.
[45] M. Yamashita, K. Shimizu, Y. Koizumi, T. Wakimoto, Y. Hamashima, T. Asakawa, M. Inai, T. Kan, *Synlett* **2016**, *27*, 2734–2736.
[46] R. Saito, T. Kuchimaru, S. Higashi, S. W. Lu, M. Kiyama, S. Iwano, R. Obata, T. Hirano, S. Kizaka-Kondoh, S. A. Maki, *Bull. Chem. Soc. Jpn.* **2019**, *92*, 608–618.
[47] C. Shu, L. Li, X.-Y. Xiao, Y.-F. Yu, Y.-F. Ping, J.-M. Zhou, L.-W. Ye, *Chem. Commun.* **2014**, *50*, 8689–8692.
[48] M. Montalti, A. Credi, L. Prodi, M. T. Gandolfi, *Handbook of Photochemistry,* CRC Press, Boca Raton, **2006.**

[49] J. Rabani, H. Mamane, D. Pousty, J. R. Bolton, *Photochem. Photobiol.* **2021**, *97*, 873–902.

[50] C. H. Langford, C. A. Holubov, *Inorg. Chim. Acta* **1981**, *53*, 59–60.

[51] Gaussian 09, Revision D.01, M. J. Frisch, G. W. Trucks, H. B. Schlegel, G. E. Scuseria, M. A. Robb, J. R. Cheeseman, G. Scalmani, V. Barone, G. A. Petersson, H. Nakatsuji, X. Li, M. Caricato, A. Marenich, J. Bloino, B. G. Janesko, R. Gomperts, B. Mennucci, H. P. Hratchian, J. V. Ortiz, A. F. Izmaylov, J. L. Sonnenberg, D. Williams-Young, F. Ding, F. Lipparini, F. Egidi, J. Goings, B. Peng, A. Petrone, T. Henderson, D. Ranasinghe, V. G. Zakrzewski, J. Gao, N. Rega, G. Zheng, W. Liang, M. Hada, M. Ehara, K. Toyota, R. Fukuda, J. Hasegawa, M. Ishida, T. Nakajima, Y. Honda, O. Kitao, H. Nakai, T. Vreven, K. Throssell, J. A. Montgomery, Jr., J. E. Peralta, F. Ogliaro, M. Bearpark, J. J. Heyd, E. Brothers, K. N. Kudin, V. N. Staroverov, T. Keith, R. Kobayashi, J. Normand, K. Raghavachari, A. Rendell, J. C. Burant, S. S. Iyengar, J. Tomasi, M. Cossi, J. M. Millam, M. Klene, C. Adamo, R. Cammi, J. W. Ochterski, R. L. Martin, K. Morokuma, O. Farkas, J. B. Foresman, D. J. Fox, Gaussian, Inc., Wallingford CT, **2013**.

[52] Avogadro: an open-source molecular builder and visualization tool. Version 1.2.0 http://avogadro.cc/

[53] GaussView, Version 6, R. Dennington, T. Keith, J. M. Millam, Semichem Inc., Shawnee Mission, KS, **2016**.

[54] S. B. Novir, *Chem. Phys. Lett.* **2017**, *690*, 86–100.

[55] A. D. Laurent, J.-M. André, E. A. Perpète, D. Jacquemin, *Chem. Phys. Lett.* **2007**, *436*, 84–88.